

CalibRefine: Deep Learning-Based Online Automatic Targetless LiDAR–Camera Calibration with Iterative and Attention-Driven Post-Refinement

Lei Cheng^a, Lihao Guo^a, Tianya Zhang^b, Tam Bang^b, Austin Harris^b, Mustafa Hajj^c,
Mina Sartipi^b and Siyang Cao^{a,*}

^aDepartment of Electrical and Computer Engineering, University of Arizona, 1200 E. University Blvd, Tucson, 85721, AZ, USA

^bCenter For Urban Informatics and Progress (CUIP), UTC Research Institute, University of Tennessee at Chattanooga, 615 McCallie Avenue, Chattanooga, 37405, TN, USA

^cElectrical Engineering Department, University of San Francisco, 2130 Fulton Street, San Francisco, 94117, CA, USA

ARTICLE INFO

Keywords:

LiDAR-camera calibration
extrinsic calibration
automatic calibration
online calibration
targetless calibration
sensor fusion
deep learning

ABSTRACT

Accurate multi-sensor calibration is essential for deploying robust perception systems in applications such as autonomous driving, robotics, and intelligent transportation. Existing LiDAR–camera calibration methods often rely on manually placed targets, preliminary parameter estimates, or intensive data preprocessing, limiting their scalability and adaptability in real-world settings. In this work, we propose a fully automatic, targetless, and online calibration framework, *CalibRefine*, which directly processes raw LiDAR point clouds and camera images. Our approach is divided into four stages: (1) a Common Feature Discriminator that trains on automatically detected objects—using relative positions, appearance embeddings, and semantic classes—to generate reliable LiDAR–camera correspondences, (2) a coarse homography-based calibration, (3) an iterative refinement to incrementally improve alignment as additional data frames become available, and (4) an attention-based refinement that addresses non-planar distortions by leveraging a Vision Transformer and cross-attention mechanisms. Through extensive experiments on two urban traffic datasets, we show that *CalibRefine* delivers high-precision calibration results with minimal human involvement, outperforming state-of-the-art targetless methods and remaining competitive with, or surpassing, manually tuned baselines. Our findings highlight how robust object-level feature matching, together with iterative and self-supervised attention-based adjustments, enables consistent sensor fusion in complex, real-world conditions without requiring ground-truth calibration matrices or elaborate data preprocessing.

1. Introduction

Reliable and accurate environment perception is becoming increasingly pivotal for advanced applications such as autonomous driving, robotics, and intelligent transportation systems. High-quality perception is essential for making well-informed decisions and ensuring safe, efficient operations. However, relying on a single sensor often presents significant challenges (Lv et al., 2021; Sengupta et al., 2022). For instance, cameras provide rich color and texture information (Berrio et al., 2021) but are highly sensitive to lighting conditions and can struggle with depth estimation, especially in poorly illuminated or rapidly changing environments (An et al., 2024). Conversely, LiDAR sensors offer precise 3D geometric information (Zhang and Rajan, 2022) and are robust to illumination variations, yet they can be more expensive and may suffer from reduced performance under adverse weather conditions (Northrop et al., 2022). Consequently, multi-sensor fusion has emerged as a practical strategy to leverage the complementary strengths of various sensing modalities (Cui et al., 2021; Ye et al., 2021; Cheng et al., 2024). Among these, camera–LiDAR fusion stands out for its ability to integrate high-resolution visual details with accurate depth measurements (Jiao et al., 2023). Despite the evident benefits, the success of sensor fusion fundamentally hinges on accurate inter-sensor calibration (Duan et al., 2023; Yoon et al., 2021). In fact, any imprecision or unreliability in this calibration process can severely degrade the performance of downstream perception tasks, leading to erroneous object detection, flawed localization, and ultimately compromised system reliability.

*Corresponding author

✉ leicheng@arizona.edu (L. Cheng); caos@arizona.edu (S. Cao)

ORCID(s):

Calibration, as a critical requirement in ensuring accurate data fusion from multiple sensors, is commonly divided into three categories: intrinsic, extrinsic, and temporal calibration (Peršić et al., 2021). Intrinsic calibration focuses on determining each sensor's internal parameters and is often provided by the manufacturer or derived from well-established procedures (Lv et al., 2022; Domhof et al., 2021). Temporal calibration estimates the constant offset between measurement instants and timestamps (Yuan et al., 2022), typically caused by jitter (random message delays), skew (differences in clock rates), sampling-frequency mismatches, or communication delays (Rehder et al., 2016). In practice, temporal calibration can be addressed either through hardware synchronization—where all sensors share a common clock—or through software-based synchronization approaches, such as approximate time synchronization (Yeong et al., 2021), which can align data by analyzing timestamp differences. Although intrinsic and temporal calibrations are vital, they are generally managed separately under controlled conditions and can often achieve satisfactory results. Consequently, in multi-sensor systems, the primary challenge shifts to extrinsic calibration—also referred to as spatial calibration or sensor registration—which involves determining the relative spatial transformations among sensor coordinates (Domhof et al., 2019; Qiu et al., 2023; Cheng et al., 2023). In the case of LiDAR–camera systems, extrinsic calibration fundamentally involves collecting corresponding points in both the LiDAR and camera coordinate frames (Cheng et al., 2023; Li et al., 2023) and using these correspondences to compute the rigid-body transformation matrix that maps one coordinate system to the other (Pandey et al., 2012; Park et al., 2020).

Depending on how these point correspondences are obtained, extrinsic calibration methods can be classified along several axes. For instance, target-based methods rely on carefully designed calibration artifacts such as checkerboards or fiducial markers to ensure accurate feature correspondence (Xiao et al., 2024). While these can deliver high-precision correspondences, they demand considerable effort in terms of setup, controlled environment preparation (Cheng and Cao, 2023), and the repetitive placement of targets (Cheng et al., 2023)—factors that are often impractical or costly in real-world applications. By contrast, targetless approaches dispense with dedicated calibration objects and instead exploit naturally occurring features in the environment (Cheng and Cao, 2023; Chen et al., 2022). This eliminates the overhead of managing physical targets and can be more adaptable to diverse scenarios, though it may pose challenges if the environment offers insufficient or indistinct features. A second dimension pertains to whether correspondence collection is manual or automatic. Manual calibration typically requires an operator to identify or verify matching points across sensors, potentially achieving high accuracy at the expense of significant time and labor (Yin et al., 2023). This approach lacks scalability, especially in large-scale or real-time deployments. Automatic calibration, on the other hand, autonomously extracts and matches features (Sun et al., 2022b; Zhang et al., 2023a), thus minimizing human involvement (Li et al., 2023). Although it hinges on the robustness of detection and matching algorithms, its reduced labor demands and potential for continuous operation make it highly appealing for applications where speed and scalability are paramount. Finally, calibration can be performed offline or online (Schneider et al., 2017; Zhu et al., 2023; Shi et al., 2020). Offline processes usually operate on batched data, allowing for extensive optimization and generally delivering precise results. However, offline methods cannot adapt to real-time sensor shifts, environmental changes, or hardware reconfigurations. In contrast, online calibration continuously updates transformation parameters as new sensor data arrives, accommodating dynamic conditions but introducing additional computational and algorithmic complexity.

Given these trade-offs, a fully automatic, targetless, and online calibration paradigm combines the most desirable attributes—removing cumbersome calibration objects, eliminating the need for human intervention, and adapting in real time to changing environments. Yet achieving all three simultaneously presents significant challenges, particularly in feature detection and correspondence matching. Nevertheless, recent advances in deep learning—especially in robust feature extraction and cross-modal matching—have opened up new pathways toward achieving this.

Current automatic, targetless, and online calibration methods for LiDAR–camera systems remain scarce, and those that do exist often exhibit significant drawbacks. Motion-based methods (Petek et al., 2024; Park et al., 2020; Sun et al., 2022a), for instance, either require extra hardware—such as camera- and LiDAR-based odometry systems—or impose constraints ill-suited to many real-world applications. Hand–eye calibration (Ou et al., 2023; Sun et al., 2022a), although well-established, is notoriously cumbersome and time-consuming, demanding multiple sensor poses that are difficult to obtain accurately in real-world dynamic scenarios where objects are in motion. Additionally, hand–eye calibration is ill-suited for static sensor setups, such as those mounted on vehicles or fixed traffic infrastructure. Edge-based calibration approaches (Li et al., 2024; Yuan et al., 2021; Yin et al., 2023; Zhang and Rajan, 2022; Zhang et al., 2023b) attempt to align object edges detected by the sensors, but matching edges is inherently difficult because object boundaries are often arbitrary and appear markedly different between LiDAR and camera modalities. Mutual information–based methods (Pandey et al., 2012; Taylor and Nieto, 2013; Koide et al., 2023) that often rely on reflectance intensities are similarly

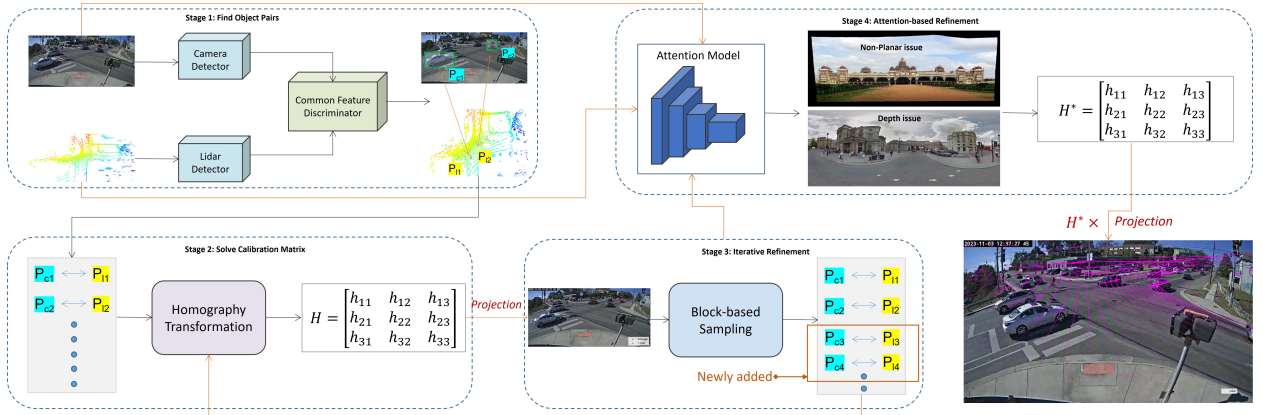


Figure 1: Work-Flow of the Proposed CalibRefine Framework for Fully Automatic Online Targetless LiDAR-Camera Calibration.

unreliable because LiDAR reflectance varies across materials and surfaces, while camera pixel intensities are heavily influenced by lighting conditions. Deep learning methods that directly regress calibration parameters—exemplified by RegNet (Schneider et al., 2017) and its variants (Zhu et al., 2023; Lv et al., 2021; Xiao et al., 2024; Duan et al., 2024; Shi et al., 2020; Iyer et al., 2018; Shang and Hu, 2022)—need an initial calibration to project LiDAR data into the image plane, resulting in a "projected LiDAR depth map". While innovative, this approach has several limitations. First, it relies on an initial calibration, which is typically obtained through manual intervention or empirical estimates based on the sensor setup, reducing generalizability. Second, the use of projected LiDAR depth maps heavily emphasizes image data, as LiDAR point clouds are sparse compared to image pixels. This results in extracted features being dominated by image characteristics, effectively sidelining valuable LiDAR information. Lastly, directly regressing calibration matrices is akin to solving an unconstrained task within constrained optimization, which is computationally challenging for current neural networks. Such models also suffer from limited generalization and are incompatible with real-time requirements due to their computational overhead. Moreover, most existing methods fail to fully leverage the already advances in object detection and feature extraction achieved in the respective domains of LiDAR and camera data processing. While some approaches utilize semantic segmentation (Sun et al., 2022a; Luo et al., 2024; Jiang et al., 2021), they often focus solely on image-based segmentation, which is computationally expensive and offers no significant advantage over object detection for calibration tasks.

In light of these limitations, we present a fully automatic, targetless, online calibration framework (Fig. 1), *CalibRefine*, that utilizes raw, unmodified LiDAR point clouds and camera images, avoiding any prior knowledge or preprocessing, such as initial calibration or projected depth maps. Instead of relying on ground-truth calibration matrices, our method employs a supervised phase for coarse calibration (using only object-level labels) followed by a self-supervised post-refinement stage. First, we leverage robust object detection algorithms—YOLOv8 (Jocher, 2023) for camera images and an octree change detection (Strawlab, 2023)-plus-DBSCAN pipeline for LiDAR data—to detect and extract individual objects from each sensor's output. A Common Feature Discriminator is then trained to match these object instances by learning more comprehensive and distinctive object-level features, going beyond simple edge features, as shown in Fig. 2. It leverages three complementary features: (1) relative positions within each sensor's frame, (2) appearance embeddings, extracted using ResNet (He et al., 2015) for camera data and PointNet++ (Qi et al., 2017) for LiDAR data, and (3) object classification information, to offer robust cross-sensor object matching capabilities. These matched objects provide a pool of reliable point correspondences, from which we compute a coarse calibration matrix using a homography-based approach. Recognizing that the Common Feature Discriminator may not achieve perfect accuracy in object matching, we enhance calibration precision through two online refinement processes. The iterative optimization-based refinement projects LiDAR points onto the camera plane, matches them with camera points using a greedy bipartite graph algorithm, and refines the calibration matrix every N frames based on reprojection error improvements. The attention-based refinement utilizes a Vision Transformer (Dosovitskiy et al., 2021) to perceive global distortion features from images, effectively mitigating the limitations of homography calibration caused by non-planar surfaces and depth variations. Furthermore, it incorporates a cross-attention network to compute weighted interactions between image pixels (queries) and LiDAR points (keys and values), establishing

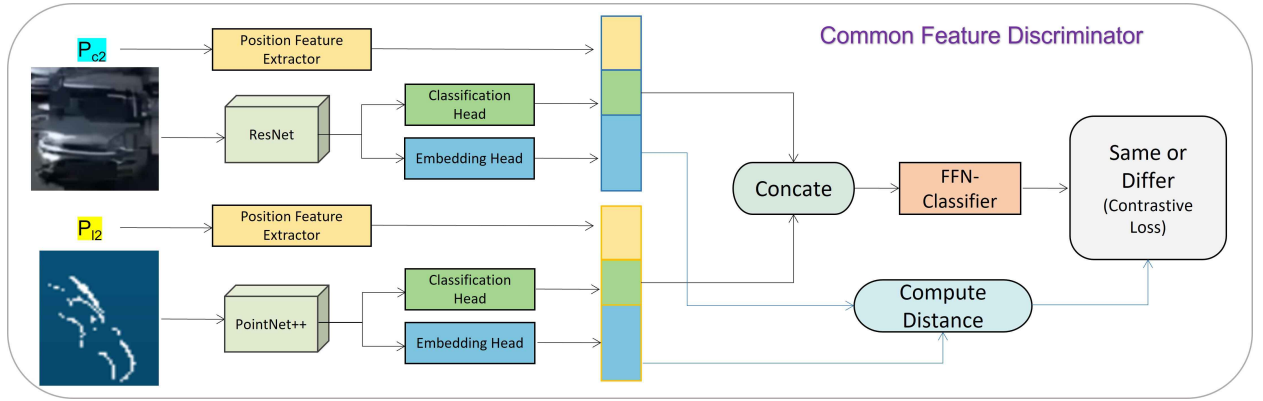


Figure 2: Overall Structure of the Common Feature Discriminator.

robust spatial correspondences and achieving further refinement of the calibration matrix. Crucially, our framework bypasses the pitfalls of direct matrix regression and the need for projected LiDAR maps, and eliminates the reliance on heuristic preprocessing or manually labeled calibration matrices, offering a more principled, data-driven pipeline that is both computationally efficient and adaptable in real-time. By integrating domain-specific mature object detection methods, a reliable discriminator to identify cross-sensor correspondences, and dual-stage refinement, our approach bridges the existing research gap, achieving a stable and accurate LiDAR–camera calibration that is truly automatic, targetless, and online. Our contributions are summarized as follows:

1. **Fully Automatic, Targetless, and Online Calibration Framework:** We propose a novel calibration framework that directly processes raw LiDAR point clouds and camera images, eliminating the need for heuristic preprocessing, manually labeled calibration matrices, or initial calibration. This ensures generalizability and adaptability across diverse scenarios.
2. **Common Feature Discriminator for Accurate Cross-Sensor Matching:** Our method introduces a deep learning–based Common Feature Discriminator to robustly identify shared object features across sensors by leveraging relative positions, appearance embeddings, and classification information, enabling precise object correspondences even in real-world environments.
3. **Coarse-to-Fine Calibration Strategy with Dual Refinement Processes:** The framework adopts a two-stage calibration approach, combining a homography-based coarse calibration with iterative refinement and attention-based refinement methods. These processes improve calibration accuracy in real-time, addressing challenges such as non-planar surfaces and dynamic conditions.

The remainder of this paper is organized as follows: Section 2 reviews the related works. Section 3 presents the proposed method in detail. Section 4 discusses the experimental results and analysis. Finally, Section 5 concludes the paper and outlines potential avenues for future research.

2. Related Works

Extrinsic calibration methods for LiDAR–camera systems can generally be divided into two categories: target-based and targetless approaches. Target-based calibration relies on specially designed calibration targets and is thus commonly associated with manual, offline procedures, although some automated methods do exist. In contrast, targetless methods extract features directly from natural scenes, making them well-suited for automatic, online calibration.

2.1. Target-based Calibration

Target-based calibration methods rely on the use of custom-designed calibration targets to extract corresponding features from the data of different sensors, enabling the calculation of extrinsic parameters. Beltrán et al. (Beltrán et al., 2022) propose a method for calibrating extrinsic parameters between LiDARs and cameras (monocular or stereo) of different modalities. The approach involves two stages: extracting reference points from a custom-designed

calibration target and determining the optimal rigid transformation by registering these point sets. The calibration target, fabricated using a CNC machine, features four circular holes to utilize geometric discontinuities in LiDAR and stereo point clouds, along with four ArUco markers placed at the corners for inferring 3D information from monocular images. Fu et al. (Fu et al., 2019) propose a LiDAR–camera calibration method using multiple chessboards placed in various poses. A stationary LiDAR scan captures the chessboards, and the camera is moved to obtain sequential images for reconstructing a 3D visual point cloud. The extrinsic parameters are then calculated by aligning the 3D visual points with the LiDAR scan using a tightly coupled graph optimization method. Zhang et al. (Zhang et al., 2023a) introduce the $L^2V^2T^2Calib$ method, which uses a four-circular-holes board as a calibration target. The centers of the circles serve as common features, detectable by sparse and dense LiDAR, repetitive and non-repetitive scanning LiDAR, as well as visual and thermal cameras. The method employs template matching for automatic target detection and calculates the calibration matrix by minimizing the 2D reprojection error. Koo et al. (Koo et al., 2022) propose a method to formulate analytic plane covariances from a 2D checkerboard planar target image, quantifying the weighting of objective functions and enhancing camera–LiDAR extrinsic calibration performance. The method uses a typical objective function based on plane feature correspondences between the camera and LiDAR. For each checkerboard image, the 3D transformation between the camera and checkerboard coordinate frames is computed using the checker square length and the PnP algorithm. Li et al. (Li et al., 2022) address the challenge of establishing common feature correspondences between sparse LiDAR point clouds and monocular images by designing a novel calibration board featuring checkerboard grids and circular holes. The extrinsic parameters are automatically determined by matching the centers of the circular holes extracted from both images and heterogeneous LiDAR scans. Huang et al. (Huang et al., 2024) propose a novel calibration method using a uniquely designed acrylic checkerboard that allows LiDAR beams to pass through the white grids and reflect off the black grids. This design reduces the size of the calibration board, enabling calibration at close distances while ensuring sufficient corresponding features can be extracted from both LiDAR scans and images to achieve accurate calibration results. Itami et al. (Itami and Yamazaki, 2020) propose an improved calibration method for a 2D LiDAR and camera system, utilizing a simple checkerboard target and a vertically rotating platform. This approach addresses a common drawback in LiDAR calibration with checkerboards—the sensitivity to checkerboard poses—by enabling more consistent and robust calibration results. Toth et al. (Tóth et al., 2020) introduce an automatic calibration method using spheres for LiDAR and camera calibration. Sphere centers are independently determined from LiDAR point clouds using RANSAC and LSQ regression and from camera images via edge detection and ellipse fitting. The extrinsic parameters of the LiDAR–camera pair are then determined through center point registration. Verma et al. (Verma et al., 2019) propose an automated method for extrinsic calibration between a camera and LiDAR using a checkerboard as a reference. The calibration board’s center point and normal vector are automatically extracted from the LiDAR point cloud by leveraging its geometric properties. Corresponding features in the camera image are derived from the camera’s extrinsic matrix. Once feature correspondences are established, a Genetic Algorithm is employed to achieve a globally optimal calibration result.

Despite their high precision, target-based methods have notable limitations. They require meticulous target preparation, often involving custom-designed and precisely fabricated targets, as well as specific setups in controlled environments. These constraints reduce their flexibility and scalability, particularly in dynamic or large-scale scenarios. Moreover, these methods generally cannot handle runtime decalibrations, a frequent occurrence in real-world applications, potentially compromising the accuracy and reliability of the calibration results.

2.2. Targetless Calibration

Targetless methods eliminate the need for manually placed dedicated calibration targets by detecting and matching naturally occurring features observable by both sensors to establish correspondences, making them more suitable for fully automatic online calibration. Depending on the type of features (or discriminative information) extracted from the scene, these approaches can be broadly categorized into motion-based, edge alignment-based, mutual information-based, and deep learning-based methods.

2.2.1. Motion-based Calibration

Petek et al. (Petek et al., 2024) introduce MDPCalib, an automated camera–LiDAR extrinsic calibration approach that requires no dedicated targets. Their method employs visual and LiDAR odometry to generate two sensor motion paths, which are aligned via a non-linear optimization for coarse registration. This coarse alignment then initializes a learning-based 2D–3D point correspondence algorithm, yielding dense matches between image and point cloud spaces. Finally, camera–LiDAR calibration is formulated as an optimization problem that minimizes costs derived from sensor

motion and point correspondences, resulting in accurate extrinsic parameters. Park et al. (Park et al., 2020) propose a LiDAR-camera calibration method that leverages each sensor's motion, which is estimated via LiDAR odometry and visual odometry. From the resulting trajectories, sets of relative transformations are extracted. By analyzing these pairs of relative transformations in both the LiDAR and camera coordinate frames, the method derives a closed-form solution for the LiDAR-camera extrinsic calibration. Yoon et al. (Yoon et al., 2021) present a targetless approach for calibrating multiple camera-LiDAR systems by leveraging object pose estimation. First, an initial calibration is generated by registering the LiDAR point cloud with an up-to-scale Structure-from-Motion (SfM) point cloud, linking corresponding instance segments in the image and point cloud domains. Based on these correspondences, a color appearance model is constructed for each object. Subsequently, iterative region-based object pose estimation is performed using the initial pose, mesh, and color appearance models, thereby refining the extrinsic parameters for multiple sensors. Some motion-based (or pose-based) methods rely on hand-eye calibration. For example, Ou et al. (Ou et al., 2023) propose a targetless LiDAR-camera calibration method leveraging cross-modality structure consistency to address the degeneration issue of hand-eye calibration when sensor motions lack sufficient rotation. Their approach uses visual and LiDAR SLAM to estimate camera and LiDAR poses from the collected data. Hand-eye calibration is then applied to compute an initial extrinsic matrix, which is further refined through a global optimization process to achieve the optimal extrinsic parameters.

These methods, while effective in leveraging sensor motion or pose data for extrinsic calibration, have notable limitations. They rely heavily on accurate motion estimation, which can be challenging in scenarios with noisy data or insufficient sensor motion, such as limited rotation. Additionally, these methods often require complex preprocessing steps, such as odometry or SLAM-based pose estimation, which may introduce errors or computational overhead. Furthermore, some approaches that rely on hand-eye calibration are prone to degeneration under specific motion patterns, such as linear trajectories with minimal rotational movement, further limiting their applicability in diverse real-world scenarios.

2.2.2. Edge Alignment-based Calibration

Zhang et al. (Zhang and Rajan, 2022) propose Multi-FEAT (Multi-Feature Edge AlignmentT), a targetless approach for camera-LiDAR extrinsic calibration. The method transforms the 2D (camera)-3D (LiDAR) calibration problem into a 2D-2D calibration problem using a cylindrical projection model. By leveraging various LiDAR features, it reconstructs edges from the sparse LiDAR point cloud more effectively. A cost function is designed to align the edge intensities of camera image edges with the edge probabilities derived from the multi-feature LiDAR point cloud. The unknown extrinsic parameters are then estimated using a gradient ascent optimization method. Li et al. (Li et al., 2024) introduce EdgeCalib, an edge-based method for automatic targetless calibration of LiDARs and cameras in real-world scenarios. The approach utilizes edge features to establish reliable correspondences between images and point clouds. The Segment Anything Model is employed to extract stable and robust image edge features, while a multi-frame weighting strategy filters features and reduces environmental dependency. Accurate extrinsic parameters are then estimated by enforcing constraints on the edge correspondences. Yuan et al. (Yuan et al., 2021) propose an automatic extrinsic calibration method designed for targetless environments. The system extracts natural edge features from both images and point clouds and minimizes the reprojection error to achieve calibration. The method includes an analysis of the constraints imposed by edge features and evaluates the impact of edge distribution on calibration accuracy. To enhance performance, they introduce an efficient LiDAR edge extraction technique based on point cloud voxel cutting and plane fitting.

Edge alignment-based calibration methods face inherent challenges due to the difficulty of matching edges between LiDAR and camera data. Object boundaries are often arbitrary, making it challenging to define consistent and reliable edge features. Furthermore, the differences in sensing modalities result in significant variations in how edges are represented, as LiDAR captures sparse geometric structures while cameras capture dense visual information. These discrepancies can lead to mismatched features, reducing the accuracy and robustness of the calibration process.

2.2.3. Mutual Information-based Calibration

Pandey et al. (Pandey et al., 2012) address the automatic, targetless extrinsic calibration of a 3D LiDAR and camera system using a mutual information (MI) framework. The algorithm registers intensity information from the camera with reflectivity information from the LiDAR. Calibration parameters are estimated by maximizing the mutual information between the sensor-measured surface intensities, enabling accurate cross-modal alignment. Taylor et al. (Taylor and Nieto, 2013) propose an automatic calibration method for camera-LiDAR systems using normalized

mutual information. The approach compares camera images with LiDAR scans of the same area. A camera model incorporating orientation, location, and focal length is used to generate a 2D LiDAR image, where pixel intensities represent features of the LiDAR scan. Particle swarm optimization is then applied to maximize the normalized mutual information and determine the optimal calibration parameters.

Mutual information-based calibration methods have significant limitations due to their reliance on reflectance intensities. LiDAR reflectance can vary widely depending on the material properties and surface characteristics, while camera pixel intensities are highly sensitive to lighting conditions. These variations can lead to unreliable correspondences, limiting the effectiveness and accuracy of such calibration approaches.

2.2.4. Deep Learning-based Calibration

Schneider et al. (Schneider et al., 2017) introduce RegNet, the first convolutional neural network (CNN) designed to directly regress the extrinsic calibration between sensors of different modalities. The problem is framed as determining the decalibration between an initial calibration matrix and a ground truth calibration matrix. To establish correspondences, LiDAR points are projected onto the camera frame using the initial calibration matrix, creating a projected LiDAR depth image. RegNet infers the correspondence between these projected depth measurements and the RGB image, ultimately regressing the extrinsic calibration parameters. Subsequent deep learning-based methods mostly follow the RegNet paradigm. For example, Lv et al. (Lv et al., 2021) propose LCCNet (LiDAR-Camera Self-Calibration Network), an online calibration framework. LCCNet employs a cost volume layer to capture the correlation between RGB image features and the depth image projected from point clouds. The network takes as input an RGB image from a calibrated camera and a projected sparse depth image from a mis-calibrated LiDAR. It outputs a 6-DoF rigid-body transformation, representing the deviation between the initial extrinsic matrix and the ground truth extrinsic matrix. Iyer et al. (Iyer et al., 2018) introduce CalibNet, a geometrically supervised deep network for real-time estimation of the 6-DoF rigid body transformation between a 3D LiDAR and a 2D camera. The network features a novel architecture based on 3D Spatial Transformers, which solves the calibration problem by maximizing geometric and photometric consistency. It takes as input an RGB image and a sparse depth map generated from a mis-calibrated LiDAR point cloud. The training process incorporates geometric supervision by minimizing dense photometric error and dense point cloud distance error, enabling the network to accurately regress the extrinsic calibration parameters. Shi et al. (Shi et al., 2020) propose CalibRCNN (Calibration Recurrent Convolutional Neural Network) to infer a 6-DoF rigid body transformation between 3D LiDAR and 2D camera. It uses an LSTM network to extract temporal features from consecutive frames of 3D point clouds and RGB images and refines calibration accuracy with geometric and photometric losses from interframe constraints. By leveraging the correspondence between projected LiDAR depth images and RGB images, CalibRCNN learns the underlying 2D–3D geometry for improved calibration precision. Xiao et al. (Xiao et al., 2024) propose CalibFormer, an end-to-end network for automatic LiDAR–camera calibration. The approach projects the LiDAR point cloud onto the image plane using the initial extrinsic parameter and camera matrix to generate a miscalibrated LiDAR image. The network takes both camera images and LiDAR images as inputs, applying a multi-head correlation module to compute correspondences between misaligned features across different dimensions. A transformer architecture is then used to extract and enhance high-contribution correlation features. Finally, the network regresses the deviations of the calibration parameters. Some deep learning methods diverge from the RegNet paradigm and instead utilize semantic segmentation models for LiDAR–camera calibration. For example, Luo et al. (Luo et al., 2024) propose a calibration method leveraging the Segment Anything Model (SAM) without additional training. SAM is used to automatically generate segmentation masks for input images. For the point cloud, normal estimation, clustering, and intensity normalization are applied to assign attributes to each point, including intensity, normal vector, and segmentation class. The extrinsic parameters are then optimized by maximizing the consistency score of the point attributes that correspond to each mask.

Current deep learning-based calibration methods, while innovative, have notable limitations. Approaches following the RegNet paradigm require an initial calibration to project LiDAR data into the image plane, creating a "projected LiDAR depth map." This reliance on initial calibration, often obtained through manual intervention or empirical estimates, reduces the method's generalizability. Additionally, the use of projected depth maps overemphasizes image data, as the sparse nature of LiDAR point clouds results in extracted features being dominated by image characteristics, sidelining valuable LiDAR-specific information. Furthermore, directly regressing calibration matrices presents a computational challenge, akin to solving an unconstrained task within constrained optimization, which challenges the capability of current neural networks. These models also face significant computational overhead, making them unsuitable for real-time applications. Methods based on semantic segmentation models also have drawbacks, as they

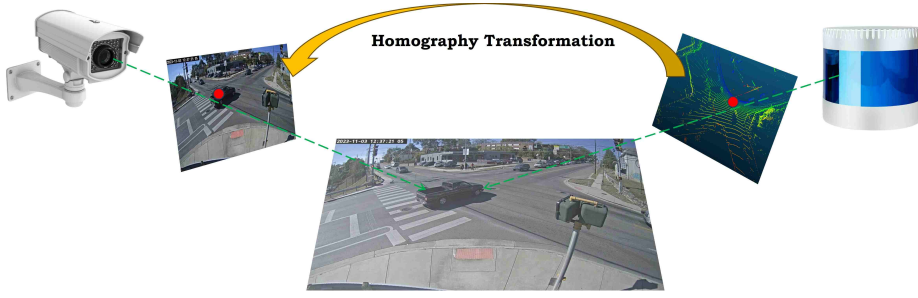


Figure 3: Illustration of Homography Transformation.

often focus solely on image-based segmentation. This approach is computationally expensive and fails to provide a significant advantage over object detection methods for calibration tasks, further questioning their practicality.

Moreover, most existing methods fail to fully exploit the advances in object detection and feature extraction developed for LiDAR and camera data processing. In contrast to existing methods, we propose a fully automatic, targetless, and online calibration framework that directly processes raw LiDAR point clouds and camera images, eliminating the need for initial calibration, projected depth maps, or heuristic preprocessing. Our approach builds on proven object detection algorithms to effectively extract objects from both sensor modalities and introduces a Common Feature Discriminator to establish correspondences by learning and matching features such as relative positions, appearance embeddings, and classification information across the two modalities. To ensure high accuracy, we introduce a two-stage refinement process: iterative refinement continuously refines the calibration by leveraging newly established correspondences, while an attention-based refinement employs a Vision Transformer and cross-attention mechanisms to address complex challenges such as non-planar surfaces, depth variations, and sensor misalignments to further refine the calibration. This method enables the direct matching of corresponding points, facilitating a straightforward, one-shot, and end-to-end calibration process between the LiDAR and camera, with improved adaptability to real-world scenarios.

3. Proposed Method

3.1. Problem Formulation

Extrinsic calibration between sensors aims to unify detections from two different sensors into the same frame of reference or coordinate system, enabling the fusion of their respective detection information. For instance, a single target appearing in both the LiDAR and camera views can provide complementary details—such as color from the camera and 3D shape from the LiDAR. Additionally, LiDAR can detect objects at greater distances than a camera might miss, compensating for the camera's detection limitations. Consequently, calibration allows for a more comprehensive and robust perception by combining the strengths of both sensors.

LiDAR–camera extrinsic calibration is typically accomplished by solving for a transformation matrix that associates a point in the image pixel coordinate system (PCS) with its corresponding point in the LiDAR coordinate system (LCS). Since points in the LCS are 3D, while those in the PCS are 2D, most existing calibration methods rely on 3D-to-2D perspective projection. However, this approach has notable drawbacks. First, it requires the camera's intrinsic matrix, adding the burden of intrinsic camera calibration, which is often performed manually, thus hindering fully automatic extrinsic calibration. Second, estimating the 3D-to-2D transformation matrix is computationally more complex and prone to instability. More importantly, for most practical applications, 3D-to-2D perspective calibration is unnecessary for achieving effective LiDAR–camera data fusion. A simpler 2D-to-2D projective calibration, where the 2D LiDAR plane is obtained by removing the Z-axis, is sufficient.

This simplification is justified for several reasons. The primary goal of calibration is to enable data fusion between the two sensors, such as associating 3D LiDAR point cloud clusters with image pixel regions for the same object. Achieving this does not require projecting the 3D LiDAR point cloud onto the image plane using a 3D-to-2D calibration matrix. Most existing methods adopt the 3D-to-2D approach as it draws from camera calibration practices that focus on 3D reconstruction. However, LiDAR–camera calibration is fundamentally different, as its focus is on data fusion, not reconstruction. By using 2D-to-2D projective calibration, where 2D LiDAR points are mapped to the image plane,

corresponding 3D LiDAR points can still be retrieved without requiring a 3D-to-2D perspective transformation. Additionally, when projecting 3D LiDAR points onto the image plane, the LiDAR data effectively becomes 2D, resulting in the loss of LiDAR's inherent 3D detection capabilities. Thus, 3D-to-2D calibration does not provide more useful information than 2D-to-2D projective calibration. Notably, while many existing methods emphasize projecting 3D LiDAR points onto the image plane, this should only serve as a visualization tool to intuitively present calibration performance, not as the calibration objective itself. The true goal of calibration should be the seamless and accurate fusion of sensor data.

Thus, we propose using planar projective transformation to achieve 2D-to-2D calibration between the 2D LiDAR plane and the camera image plane, as illustrated in Fig. 3. A planar projective transformation, or Homography, is an invertible linear transformation represented by a non-singular matrix $\mathbf{H} \in \mathbb{R}^{3 \times 3}$ (Dubrofsky, 2009). This transformation allows us to project a point in the LCS directly onto the camera image plane without requiring the camera intrinsic matrix. The relationship is expressed as:

$$\begin{bmatrix} u_l \\ v_l \\ 1 \end{bmatrix} = \mathbf{H} \begin{bmatrix} x \\ y \\ 1 \end{bmatrix} = \begin{bmatrix} h_{11} & h_{12} & h_{13} \\ h_{21} & h_{22} & h_{23} \\ h_{31} & h_{32} & h_{33} \end{bmatrix} \begin{bmatrix} x \\ y \\ 1 \end{bmatrix}, \quad (1)$$

where $\hat{P}_l = (u_l, v_l)$ is the projection of a point $P_l = (x, y)$ in the LCS onto the camera image plane PCS. Notably, the objects or points on the 2D LiDAR plane and those on the camera image plane are derived from objects or points lying on a common plane (e.g., the ground plane), as shown in Fig. 3. This alignment justifies the use of 2D Homography for LiDAR–camera calibration, as it can be considered a planar homography induced by the common plane (Szeliski, 2022). To solve for the Homography matrix, a set of N points in the LCS and their corresponding points in the PCS is required. While 4 points are theoretically sufficient to compute the matrix, more points are typically used to optimize the solution based on a specific cost function (Dubrofsky, 2009). The most widely used cost function is the minimization of the geometric reprojection error (Hartley and Zisserman, 2003; Dubrofsky, 2009), which evaluates the alignment between N projected 2D LiDAR pixel points ($\hat{P}_l = (\hat{u}, \hat{v})$) and their corresponding 2D image pixel points ($P_p = (u, v)$). Minimizing this reprojection error ensures an accurate Homography matrix for precise calibration. Specifically, the reprojection error can be measured as either the average Euclidean distance (L2 norm mean) or the root mean square error.

1. **Average Euclidean Distance (AED):** It computes the mean of the Euclidean distances between the projected points and their corresponding ground truth points. It provides a straightforward and intuitive measure of overall alignment, offering insight into the average deviation between matched points:

$$\mathcal{E}_{\text{AED}} = \frac{1}{N} \sum_{i=1}^N \|P_p^i - \hat{P}_l^i\|_2 = \frac{1}{N} \sum_{i=1}^N \sqrt{(u^i - \hat{u}^i)^2 + (v^i - \hat{v}^i)^2}. \quad (2)$$

2. **Root Mean Square Error (RMSE):** Alternatively, the reprojection error can be expressed as the root mean square error, which is more sensitive to larger deviations. By squaring the Euclidean distances before averaging, this measure amplifies the influence of outliers, ensuring that significant misalignments are effectively penalized:

$$\mathcal{E}_{\text{RMSE}} = \sqrt{\frac{1}{N} \sum_{i=1}^N \|P_p^i - \hat{P}_l^i\|_2^2} = \sqrt{\frac{1}{N} \sum_{i=1}^N [(u^i - \hat{u}^i)^2 + (v^i - \hat{v}^i)^2]}. \quad (3)$$

3.2. Method Overview

We aim to develop a framework for LiDAR–camera online automatic targetless calibration, designed to reduce human intervention, streamline sensor integration, and ensure high precision in LiDAR–camera fusion applications. Our method comprises the following stages, as shown in Fig. 1:

1. **Stage 1:** In this stage, the established LiDAR and camera detectors are utilized to detect and extract objects from their respective sensor data. Each detected object is extracted, including its center position (the bounding box center for the camera detection and the cluster center for the LiDAR point cloud). These objects are then used to train a Common Feature Discriminator, which determines whether an image object and a LiDAR object

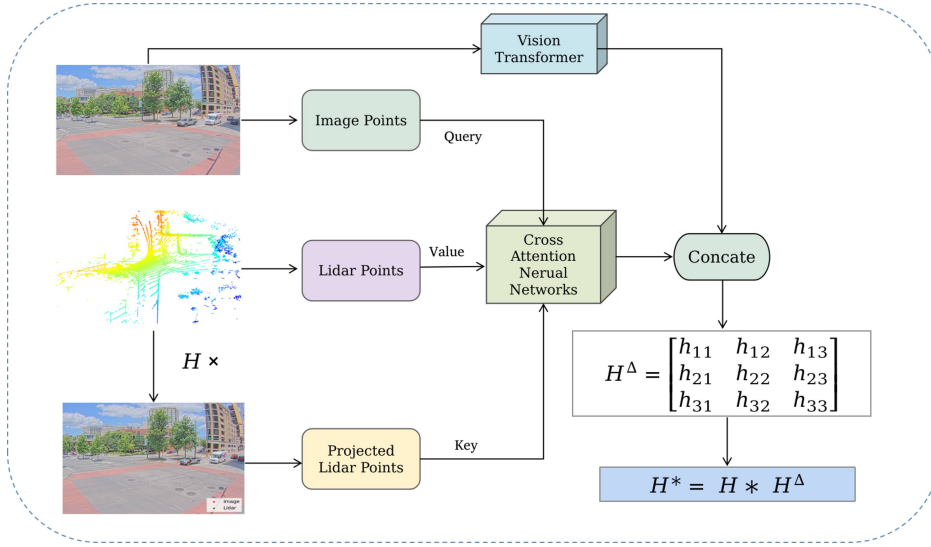


Figure 4: Schematic Overview of the Attention-based Refinement Process.

correspond to the same entity. To achieve this, the discriminator learns and compares three distinct features: Relative Positions, Appearance Embeddings, and Classification Information. These features are concatenated and passed through a feed-forward neural network (FFN) classifier, which outputs a decision on whether the objects from the two sensors are the same or different.

2. **Stage 2:** This stage involves solving the calibration matrix using the identified object pairs. A homography transformation is applied to generate a coarse initial calibration matrix (H), which establishes a preliminary correspondence between objects detected by the LiDAR and camera.
3. **Stage 3:** In this stage, an iterative refinement-based fine calibration is performed to refine the calibration matrix, considering that the Common Feature Discriminator may not precisely match all corresponding objects. The initial calibration matrix from the previous stage is used to project LiDAR data onto the camera plane, enabling the selection and construction of additional point correspondences based on distance criteria. These newly established correspondences are then used to achieve more precise calibration through iterative refinement.
4. **Stage 4:** In the final stage, attention-based refinement employs a Vision Transformer to extract global distortion features from images, effectively addressing the limitations of homography calibration caused by non-planar surfaces and depth variations. This also compensates for errors introduced by the absence of camera intrinsic matrix-based rectification. Furthermore, it integrates a cross-attention network to compute weighted interactions between image pixels (as queries), projected LiDAR points (as keys), and LiDAR points (as values), thereby capturing more accurate correspondences between LiDAR and camera data points. The model fundamentally learns and generates a correction matrix (H^Δ) to refine the initial calibration, resulting in an improved matrix (H^*) for better LiDAR–camera alignment.

3.3. Common Feature Discriminator

The key to solving the extrinsic calibration matrix, which aligns the LiDAR and camera coordinate systems, lies in identifying a sufficient number of object correspondences between the two sensor views. Although objects detected by LiDAR and cameras may appear quite different due to the disparate nature of the data (geometric point clouds versus pixel-based images), they inherently share some common characteristics:

1. **Shape:** Objects exhibit geometric shapes that can be captured as contours in camera images and point clusters in LiDAR data.
2. **Semantic Information:** Both LiDAR and camera data can reveal high-level semantic features, such as object categories (e.g., vehicles, pedestrians), that correspond across modalities.
3. **Reflection Intensity:** LiDAR measures reflection intensity based on surface material properties, while cameras capture similar information through brightness and contrast.

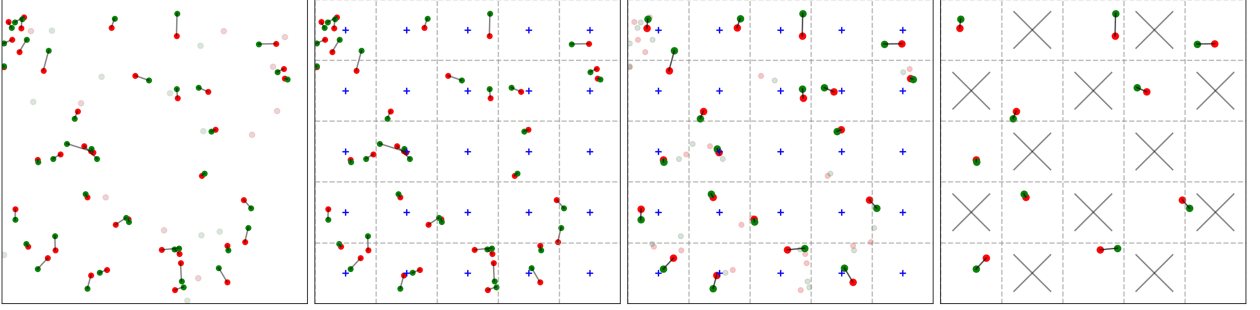


Figure 5: Block-based Sampling Strategy: 1) Project LiDAR points onto the image, identifying LiDAR-camera point pairs (red: camera, green: LiDAR); 2) Divide the image into equal-sized grids, marking centers; 3) Retain pairs whose camera point is nearest to the grid center; 4) Sample pairs at intervals of one block, discarding those in skipped blocks.

Recognizing and leveraging these shared features offers a viable approach to establishing robust correspondences (Cheng and Cao, 2025) between LiDAR and camera detections of the same objects.

To achieve this, we propose the Common Feature Discriminator, a deep learning-based model designed to leverage deep learning’s superior feature extraction capabilities to learn and extract these shared features from LiDAR and camera data, thereby enabling effective object matching and correspondence identification. The first step of our approach is to detect and crop individual objects from each sensor’s output. To this end, we employ two established object detector tailored to LiDAR and camera data, respectively: 1) *Camera-based object detection*: We adopt YOLOv8 (Jocher, 2023) for robust 2D object detection in images. This produces bounding boxes around each detected object in the camera frame. 2) *LiDAR-based object detection*: We use an octree-based change detection algorithm (Strawlab, 2023) followed by a DBSCAN clustering step to segment point cloud regions corresponding to individual objects. This yields point clusters, each hypothesized to belong to a distinct object in the LiDAR frame. Because the LiDAR and camera frames are time-synchronized, each LiDAR cluster and camera bounding box within the same timestamp can be treated as candidate object detections from two complementary modalities.

Once objects have been cropped from the LiDAR and camera data, they are fed into our proposed Common Feature Discriminator. This module is responsible for determining whether an object in the camera image and an object in the LiDAR point cloud correspond to the same physical entity. To accomplish this, the Common Feature Discriminator learns and compares three key types of features—*relative positions*, *appearance embeddings*, and *classification information*—and fuses them to produce a final similarity decision, as outlined in Fig. 2:

1. **LiDAR Feature Extraction:** Each LiDAR object (i.e., a 3D point cluster) is passed to a LiDAR backbone (e.g., PointNet++), which encodes the local and global geometric structure of the object into a latent vector. A *Classification Head* outputs the object category (e.g., car, pedestrian)—accounting for the expectation that matching objects in LiDAR and camera views should share the same class—while an *Embedding Head* produces a 128-dimensional feature capturing the object’s 3D shape and reflection intensity. These two heads thus provide both semantic consistency checks (via classification) and geometric/reflective characteristics checks (via appearance embeddings). Let \mathbf{X}_L denote the 3D point cluster associated with a LiDAR object. A PointNet++ backbone maps \mathbf{X}_L to:

$$\mathbf{z}_L = f_{\text{emb}}(\mathbf{X}_L), \quad \hat{c}_L = f_{\text{cls}}(\mathbf{X}_L),$$

where $\mathbf{z}_L \in \mathbb{R}^{128}$ is the LiDAR embedding and \hat{c}_L is the predicted class (e.g. car, truck, pedestrian).

2. **Camera Feature Extraction:** In parallel, each camera-cropped object (the pixels within its bounding box) is processed by an image backbone (e.g., ResNet). Similar to the LiDAR branch, this has a *Classification Head* that yields object categories, and an *Embedding Head* that provides a 128-dimensional representation of the geometric features (appearance embeddings) such as shape and structure. Let \mathbf{I}_C be the pixel region representing a camera-detected object. A ResNet-based backbone maps \mathbf{I}_C to:

$$\mathbf{z}_C = g_{\text{emb}}(\mathbf{I}_C), \quad \hat{c}_C = g_{\text{cls}}(\mathbf{I}_C),$$

providing the camera embedding $\mathbf{z}_C \in \mathbb{R}^{128}$ and the predicted semantic class \hat{c}_C .

3. **Position Feature Extraction:** Both LiDAR and camera objects also go through a *Position Feature Extractor*, which calculates the relative positions of objects within their respective sensor frames. This captures spatial alignment cues, allowing the model to verify if the apparent location of an object in the camera image aligns with the corresponding object’s location in the LiDAR point cloud. Each object’s 2D center, (x, y) for LiDAR and (u, v) for camera, yields:

$$\Delta \mathbf{p} = (u - x, v - y),$$

forming a *relative position vector* to capture spatial consistency across sensor views.

4. **Feature Fusion and Matching:** The three types of features—(i) *Relative Positions* derived by the Position Feature Extractor, (ii) *Appearance Embeddings* from the Embedding Heads, and (iii) *Classification Information* from the Classification Heads—are concatenated into a unified feature vector

$$\mathbf{f} = [\Delta \mathbf{p}; \mathbf{z}_L; \mathbf{z}_C; \hat{c}_L; \hat{c}_C],$$

which is then fed into a small feed-forward network (FFN) for binary classification (“Same” vs. “Differ”):

$$\hat{o} = \sigma(\text{FFN}(\mathbf{f})),$$

where σ denotes the sigmoid activation. During training, a contrastive loss \mathcal{L}_{ctr} encourages embeddings of true-matching object pairs ($\hat{o} = 1$) to remain close while pushing non-matching pairs ($\hat{o} = 0$) apart, providing additional input for the classification decision.

By jointly analyzing $\Delta \mathbf{p}$, \mathbf{z}_L , \mathbf{z}_C , and \hat{c}_L, \hat{c}_C , the Common Feature Discriminator robustly determines whether the LiDAR and camera detections refer to the same underlying object, even when the modalities present substantially different raw representations, thereby enabling the system to automatically match and associate objects across LiDAR and camera views. This module, integrated with LiDAR and camera object detectors, constitutes the foundation of an end-to-end cross-sensor object matching workflow. Specifically, time-synchronized LiDAR and camera frames are processed in parallel, and bounding boxes (camera) or point clusters (LiDAR) are cropped and fed into the discriminator to obtain pairwise correspondence labels. The resulting high-confidence matches form the cornerstone for computing the extrinsic calibration matrix that aligns the LiDAR and camera coordinate frames.

3.4. Homography-based Calibration Matrix Estimation

Once the Common Feature Discriminator identifies matched objects in the LiDAR and camera views, we extract their 2D center coordinates in each sensor’s frame to form point correspondences. Let us denote these correspondences by the set

$$\mathcal{C} = \left\{ (x_i, y_i) \leftrightarrow (u_i, v_i) \right\}_{i=1}^N,$$

where (x_i, y_i) represents the i th LiDAR object center in the 2D LiDAR plane, and (u_i, v_i) denotes the corresponding camera object center in the image plane. Given these correspondences, we estimate the 2D homography matrix $\mathbf{H} \in \mathbb{R}^{3 \times 3}$ (cf. Eq. (1)) that satisfies

$$\begin{bmatrix} u_i \\ v_i \\ 1 \end{bmatrix} \approx \mathbf{H} \begin{bmatrix} x_i \\ y_i \\ 1 \end{bmatrix}, \quad \text{for } i = 1, \dots, N.$$

To ensure robustness against erroneous matches, we employ the RANSAC algorithm (Cheng and Cao, 2023) to iteratively fit \mathbf{H} while discarding outlier correspondences. Specifically, RANSAC randomly samples a small subset $\mathcal{C}_s \subset \mathcal{C}$ of correspondences to compute a candidate \mathbf{H}_s . It then evaluates \mathbf{H}_s on the entire set \mathcal{C} by measuring the reprojection error (e.g. \mathcal{E}_{AED} or $\mathcal{E}_{\text{RMSE}}$), and repeats this process over multiple iterations. The matrix \mathbf{H} yielding the largest inlier consensus (and thus the lowest average error) is ultimately selected.

Although RANSAC mitigates outliers, clustering of correspondences can still bias the homography solution if most matches lie in a small image region. to ensure that the point correspondences used in calibration are well-distributed

Algorithm 1 Iterative LiDAR–Camera Calibration Refinement

Input: Frames $F = \{(L_i, C_i)\}$ for $i = 1 \dots T$ ▷LiDAR and camera points for T frames
InitMatrix ▷Initial calibration matrix from Common Feature Discriminator
 $N \in \mathbb{Z}$ ▷Number of frames to accumulate before recalibration
BlockSize ▷Block dimension for sampling strategy
Output: CalibMatrix* ▷Refined calibration matrix

- 1: BestMatrix \leftarrow InitMatrix ▷Set the initial calibration matrix as the best
- 2: AccumulatedPairs $\leftarrow []$ ▷List to store point correspondences
- 3: **for** $i \in \{1, 2, \dots, T\}$ **do**
- 4: projPoints \leftarrow Project(L_i , BestMatrix) ▷Project LiDAR object centers onto the camera plane
- 5: matchedPairs \leftarrow GreedyBipartiteMatch(projPoints, Points(C_i)) ▷Match points
- 6: blockFilteredPairs \leftarrow BlockBasedSampling(matchedPairs, BlockSize) ▷Select one pair per block
- 7: AccumulatedPairs.append(blockFilteredPairs) ▷Add new correspondences
- 8: **if** $i \bmod N == 0$ **then**
- 9: NewCalibMatrix \leftarrow Recalibrate(AccumulatedPairs) ▷Re-do calibration
- 10: errOld \leftarrow ComputeReprojError(BestMatrix, AccumulatedPairs)
- 11: errNew \leftarrow ComputeReprojError(NewCalibMatrix, AccumulatedPairs)
- 12: **if** errNew < errOld **then**
- 13: BestMatrix \leftarrow NewCalibMatrix ▷Update calibration if improvement is found
- 14: **end if**
- 15: **end if**
- 16: **end for**
- 17: CalibMatrix* \leftarrow BestMatrix ▷Final refined calibration matrix
- 18: **return** CalibMatrix*

across the sensor field of view—thus making the calibration results more representative and robust—we employ a *block-based sampling* approach. As illustrated in Fig. 5, the camera image plane is partitioned into an array of blocks, each of size $\delta_x \times \delta_y$ (5×5 in our case). Let

$$\Omega = \bigcup_{j=1}^J B_j$$

be the partition, where B_j is the j th block. For each block B_j , we collect any point pairs whose camera coordinates (u_i, v_i) fall inside B_j , then select exactly one representative $(x_j^*, y_j^*) \leftrightarrow (u_j^*, v_j^*)$ nearest to B_j 's center \mathbf{c}_j . This yields a spatially diverse subset

$$C' = \left\{ (x_j^*, y_j^*) \leftrightarrow (u_j^*, v_j^*) \right\}_{j=1}^J,$$

which contributes to a more robust and stable homography estimate.

By combining object-level correspondences C (or C') and outlier rejection (RANSAC) with the block-based sampling, we obtain a reliable homography-based calibration matrix $\mathbf{H}_{\text{coarse}}$. Notably, this coarse calibration method requires no manual intervention, enabling real-time online calibration that can effectively handle runtime decalibration. By integrating the Common Feature Discriminator with this homography-based approach, we achieve a fully automated calibration pipeline, which serves as an initial coarse calibration step.

It is worth emphasizing that, unlike many existing LiDAR–camera calibration methods that attempt to utilize every LiDAR point, our approach relies solely on the centers of detected objects. We adopt this strategy for two main reasons (also as explained in Section 3.1). First, since the goal of calibration is to align LiDAR objects with camera objects, using object center points is already sufficient for establishing accurate correspondences; incorporating all LiDAR points does not provide any additional benefit for object association and can actually complicate the calibration matrix estimation process. Second, even though the calibration matrix is derived from object center points only, it can still be

used to project the entire LiDAR point cloud onto the image plane. Moreover, this center-based approach naturally fits an object-level matching paradigm, especially considering that camera-detected objects lack corresponding point cloud data. By reducing the reliance on dense point sets and focusing on object centers, we gain more degrees of freedom to achieve a robust and flexible calibration outcome.

3.5. Iterative Refinement Process

While relying on the Common Feature Discriminator to establish a coarse initial calibration matrix can provide a strong starting point, it may not perfectly match every corresponding object in LiDAR and camera data. In practice, leveraging additional data points (and thus increasing redundancy and field-of-view coverage) often improves both the accuracy and robustness of calibration estimation. To that end, we propose an iterative refinement procedure that successively updates the calibration matrix by incorporating newly discovered point correspondences across multiple frames. The process (as demonstrated in Algorithm 1) unfolds as follows:

1. **Initial Calibration:** We begin by using the coarse calibration matrix obtained from coarse calibration as the initial matrix, i.e., $\mathbf{H}_0 = \mathbf{H}_{\text{coarse}}$. The LiDAR-camera point pairs identified by the Common Feature Discriminator during coarse calibration form an initial accumulated set \mathcal{A} .
2. **LiDAR-to-Camera Projection:** Let $\mathbf{H}_{\text{best}} = \mathbf{H}_0$, for each incoming frame (L_i, C_i) , where $i \in \{1, \dots, T\}$, every LiDAR object center (x_j, y_j) in L_i is projected onto the camera plane using the current best matrix \mathbf{H}_{best} :

$$\begin{bmatrix} \hat{u}_j \\ \hat{v}_j \\ 1 \end{bmatrix} = \mathbf{H}_{\text{best}} \begin{bmatrix} x_j \\ y_j \\ 1 \end{bmatrix}.$$

We then compare each projected point (\hat{u}_j, \hat{v}_j) with the camera-detected objects in C_i .

3. **Greedy Bipartite Matching:** We then form a bipartite graph between the projected LiDAR points $\{(\hat{u}_j, \hat{v}_j)\}$ and the camera-detected object centers $\{(u_i, v_i)\}$ from C_i . To expand our pool of correspondences, a greedy bipartite matching (Besser and Poloczek, 2017) associates each LiDAR point with the closest camera object (if any) based on a distance measure $d((\hat{u}, \hat{v}), (u, v))$.
4. **Correspondence Selection:** Let \mathcal{M}_i be the new candidate point pairs set from frame i . Only newly formed point pairs that fall within unoccupied or sufficiently distinct grid regions—determined using the proposed block-based sampling strategy (Fig. 5)—are retained. The resultant filtered set $\widetilde{\mathcal{M}}_i \subseteq \mathcal{M}_i$ is then added to the existing accumulated set \mathcal{A} :

$$\mathcal{A} \leftarrow \mathcal{A} \cup \widetilde{\mathcal{M}}_i,$$

effectively expanding the coverage within the sensors' field of view and enhancing the calibration robustness.

5. **Recalibration and Validation:** After accumulating every $N = 100$ frames (or another empirically chosen threshold) and gathering all associated point pairs, we re-estimate a new calibration matrix \mathbf{H}_{new} using the accumulated point pairs \mathcal{A} and the homography calibration algorithm (Section 3.4). Formally,

$$\mathbf{H}_{\text{new}} = \text{Recalibrate}(\mathcal{A}) \quad \text{via minimizing} \quad \sum_{(x,y) \leftrightarrow (u,v) \in \mathcal{A}} \varphi(\mathbf{H}, (x, y), (u, v)),$$

where $\varphi(\cdot)$ is the chosen reprojection error function (e.g. \mathcal{E}_{AED} , $\mathcal{E}_{\text{RMSE}}$). If the new matrix provides no improvement in terms of reprojection error (i.e., projected LiDAR points are not better aligned with camera objects), it is discarded; otherwise, it updates the best matrix $\mathbf{H}_{\text{best}} \leftarrow \mathbf{H}_{\text{new}}$.

6. **Iterate:** We repeat Steps 2–5 for all subsequent frames $i + 1, i + 2, \dots$ until reaching the final time step T . This iterative loop gradually refines the calibration matrix by incorporating newly validated point correspondences.

By systematically incorporating additional correspondences at each iteration, this optimization loop converges toward a more robust calibration matrix. It maintains the practical advantages of the initial deep learning-based matching while progressively enhancing accuracy through redundancy and extended spatial coverage. Moreover, its iterative

Table 1
Performance of Common Feature Discriminator

Metric	Dataset 1	Dataset 2
Binary Classification Accuracy (%)	98.00	92.50
Image Classification Accuracy (%)	82.80	72.00
LiDAR Classification Accuracy (%)	87.34	85.50

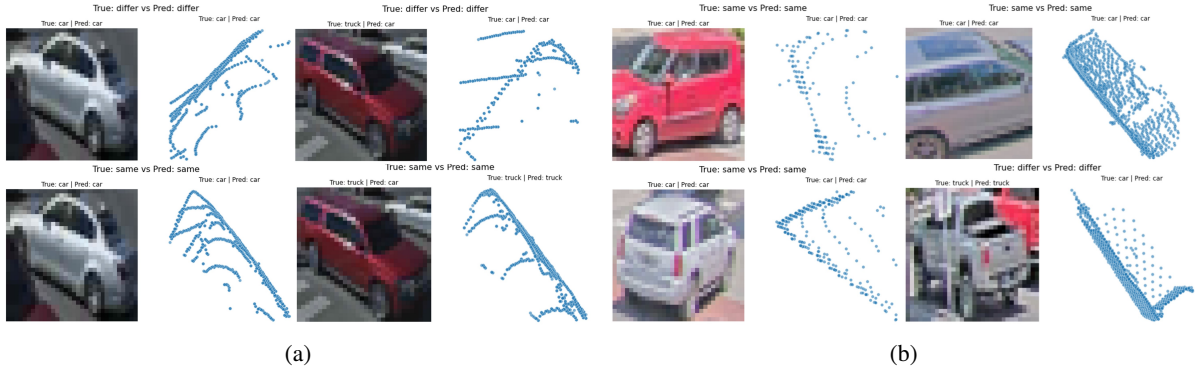


Figure 6: Test Examples with Common Feature Discriminator: (a) Results on Dataset 1, (b) Results on Dataset 2.

nature naturally accommodates runtime changes in the environment, thus helping to mitigate potential decalibration over long-term operation.

It is worth noting that we opt for a greedy bipartite matching (Besser and Poloczek, 2017) approach rather than the more popular Hungarian algorithm for several practical reasons. Ideally, each LiDAR detection would correspond to exactly one camera detection, and bipartite graph matching would produce a one-to-one mapping that minimizes the overall matching cost. However, real-world conditions deviate from this ideal scenario: variations in field of view and detection capabilities can lead to certain objects being detected by only one sensor. For example, LiDAR may capture distant objects outside the camera’s range, whereas a camera may pick up small or reflective objects that the LiDAR cannot reliably detect. Given these discrepancies, the goal of bipartite graph matching is to identify the best subset of matching pairs, without forcing all detections from both sensors to be paired. Greedy bipartite matching is well-suited to this task, as it prioritizes finding and accumulating the lowest-cost matches while allowing some objects to remain unmatched if no suitable pair exists. In contrast, the Hungarian algorithm aims for an optimal, one-to-one, and complete assignment—i.e., pairing every detection from both sensors—an assumption that does not hold in many real-world LiDAR–camera detections. Such forced one-to-one pairings can degrade matching quality when unmatchable objects are forced to pair with unrelated detections.

3.6. Attention-based Refinement Process

While homography-based calibration can provide a reasonable initial solution, it relies on planar assumptions and may introduce non-negligible errors in real-world environments with complex depth variations. To address these limitations and further refine the calibration, we adopt an attention-based deep learning model that produces a correction matrix \mathbf{H}^Δ , as illustrated in Fig. 4. Once trained, the refined calibration is computed as

$$\mathbf{H}^* = \mathbf{H} \times \mathbf{H}^\Delta,$$

where \mathbf{H} is the calibration matrix from earlier stages, and \mathbf{H}^Δ compensates for non-planar distortions, lens imperfections, and other real-world discrepancies.

1. **Vision Transformer for Global Distortion Features:** Unlike purely convolutional networks, a *Vision Transformer* (ViT) employs self-attention to capture global cues from the input image. Let \mathbf{I} denote the image, partitioned into patches $\{\mathbf{p}_1, \dots, \mathbf{p}_m\}$. The ViT encodes each patch as a token $\mathbf{t}_i = f_{\text{ViT}}(\mathbf{p}_i)$, and uses multi-head

attention to capture long-range dependencies:

$$\text{Attn}(\mathbf{Q}, \mathbf{K}, \mathbf{V}) = \text{Softmax}\left(\frac{\mathbf{Q}\mathbf{K}^\top}{\sqrt{d}}\right)\mathbf{V},$$

where d is the token dimension. By aggregating information across patches, the ViT reveals global distortion features that a simple planar model cannot accommodate. This capability helps mitigate inaccuracies stemming from homography's planar assumptions or the absence of camera-intrinsic rectification.

2. **Cross-Attention for LiDAR–Camera Correspondences:** To establish more accurate correspondences between LiDAR and camera data, we integrate a cross-attention mechanism that takes:

- *Queries* \mathbf{Q}_c from image points, $\{(u_i, v_i)\}_{i=1}^N$.
- *Keys* \mathbf{K}_c from projected LiDAR points, $\{\hat{u}_j, \hat{v}_j\}_{j=1}^M$, derived by transforming each LiDAR 2D coordinate (x_j, y_j) via \mathbf{H} .
- *Values* \mathbf{V}_c from the original LiDAR points, $\{(x_j, y_j, z_j)\}_{j=1}^M$, retaining full 3D spatial information.

By computing weighted interactions $\mathbf{A}_{\text{cross}}$ between these queries and keys,

$$\mathbf{A}_{\text{cross}} = \text{Softmax}\left(\frac{\mathbf{Q}_c \mathbf{K}_c^\top}{\sqrt{d}}\right)\mathbf{V}_c,$$

the model effectively links each image point with its corresponding 3D LiDAR counterpart. This cross-modal attention captures more accurate 2D–3D relationships and refines the camera–LiDAR alignment beyond what a purely homography-based approach can achieve.

3. **Learning the Correction Matrix:** Let \mathbf{z}_{ViT} be the output tokens from the Vision Transformer and $\mathbf{A}_{\text{cross}}$ be the cross-attention output. We concatenate these to form a feature vector

$$\mathbf{f} = [\mathbf{z}_{\text{ViT}}, \mathbf{A}_{\text{cross}}],$$

which is passed through additional layers $g(\cdot)$ that regress a 9-dimensional vector $\boldsymbol{\theta}$, representing the correction matrix:

$$\boldsymbol{\theta} = g(\mathbf{f}), \quad \mathbf{H}^\Delta = \text{Reshape}(\boldsymbol{\theta}) \in \mathbb{R}^{3 \times 3}.$$

The final refined homography is

$$\mathbf{H}^* = \mathbf{H} \times \mathbf{H}^\Delta.$$

During training, a self-supervised objective seeks to minimize the reprojection error between the \mathbf{H}^* -projected LiDAR points and their corresponding image coordinates, thus driving \mathbf{H}^Δ to compensate for any non-planar misalignments left by the base homography.

By combining global image-level context (from the Vision Transformer) with precise, point-level cross-attention (between image queries, projected LiDAR keys, and LiDAR values), the model robustly captures spatial relationships in both 2D and 3D domains. This synergy accommodates complex depth variations and non-planar surfaces, corrects inaccuracies introduced by simpler homography assumptions, and increases resilience to real-world imaging conditions, such as partial occlusions or unrectified camera images without intrinsic parameters. Another key advantage of our proposed attention-based deep learning model is that it can be trained in a self-supervised manner, without requiring explicit annotation of LiDAR–camera correspondences. Specifically, the model iteratively adjusts the homography matrix by comparing projected LiDAR points against their nearest image correspondences, allowing these implicit pairings to serve as the supervisory signal. Consequently, the model is able to autonomously learn a correction matrix \mathbf{H}^Δ that minimizes reprojection errors—i.e., discrepancies between the LiDAR points (projected into the camera frame) and their corresponding image points. By relying on these implicit constraints within the data itself—rather than manual annotations—our approach eliminates human effort and intervention thus enabling real-time, online LiDAR–camera calibration. It is worth noting that a relatively accurate initial matrix is crucial for effective self-supervised training. Therefore, our attention-based refinement is strategically positioned after the iterative refinement process, ensuring a robust starting point for the training.

4. Experimental Results and Analysis

4.1. Sensor Setup and Data Collection



Figure 7: Sample Street-View of the Sensor Setup at the Intersection for Dataset 1.

Dataset 1: The first dataset was collected at the intersection of M.L.K. Boulevard and Central Avenue in the Chattanooga Smart Corridor, where a comprehensive two-hour synchronized dataset was gathered using multiple sensor types. The sensor setup consisted of 32-channel LiDAR systems mounted on utility poles at the intersection corners, as illustrated in Fig. 7. These LiDAR units operate with a detection range of 0.05 to 120 meters and are complemented by integrated video cameras. The dual-sensor approach combines precise LiDAR spatial measurements with video footage, providing both quantitative data and visual context for validating observations.

Dataset 2. The second dataset was collected at an urban intersection in downtown Chattanooga, specifically at Georgia Avenue and M.L.K. Boulevard. This site was chosen for its high traffic volume and diverse mix of road users. Similar to Dataset 1, a LiDAR-camera system was employed to collect the data; LiDAR scans and camera images were synchronized via ROS and stored in *ROSbag* files with precise timestamps. This setup ensures accurate alignment of multi-modal data, thereby facilitating the investigation of cross-sensor calibration.

4.2. Deep Learning Model Training

4.2.1. Data Annotation and Dataset Generation

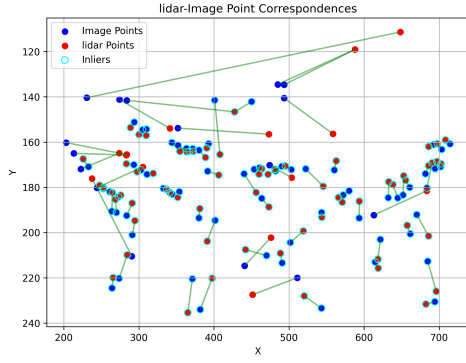
We developed a multi-sensor annotation toolkit designed for efficiently labeling common objects captured by both camera images and point cloud data, with applications in autonomous driving and intelligent transportation research. This toolkit integrates both automatic and manual annotation methods, thereby optimizing the labeling process while ensuring high-quality datasets.

For bounding box generation, the toolkit employs two primary approaches. In camera image annotation, it first utilizes a YOLO-based object detection algorithm to automatically generate bounding boxes and then allows users to manually draw boxes for precise labeling. For LiDAR point cloud data, the toolkit automatically extracts the background through preprocessing algorithms and uses DBSCAN clustering to detect objects and generate initial bounding boxes, which can subsequently be refined manually if necessary.

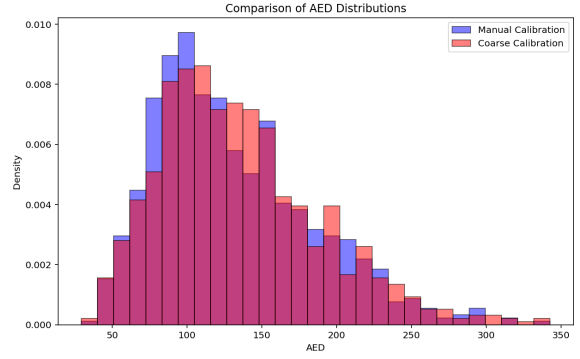
Furthermore, once detections from both camera and LiDAR are available, the toolkit offers a dual-view visualization interface that enables users to match identical objects across the two sensor modalities. Using this system, we annotated the two datasets described above: Dataset 1 consists of 1200 frames, of which 800 frames were annotated, resulting in a total of 5,815 labeled identical objects; Dataset 2 consists of 600 frames, with 200 frames annotated and a total of 619 labeled identical objects.

4.2.2. Training Details

The Common Feature Discriminator and the Attention-based Model were both trained from scratch on the UArizona High-Performance Computing Platform, utilizing a computational setup that included a single Nvidia 32GB V100S GPU and an AMD Zen2 processor with 5 cores and 30GB of RAM. The training was implemented using PyTorch 2.0 as the deep learning framework. The optimization process was carried out using the Adam optimizer, configured with a momentum of 0.937 and a weight decay of 5×10^{-4} . A cosine learning rate schedule was employed to dynamically adjust the learning rate, beginning with an initial learning rate of 0.001, warming up with a ratio of 0.05,



(a)



(b)

Figure 8: (a) Point Pairs Identified by the Common Feature Discriminator on Dataset 1. (b) Comparison of \mathcal{E}_{AED} Distributions on Dataset 1 between Manual Calibration and Coarse Calibration.

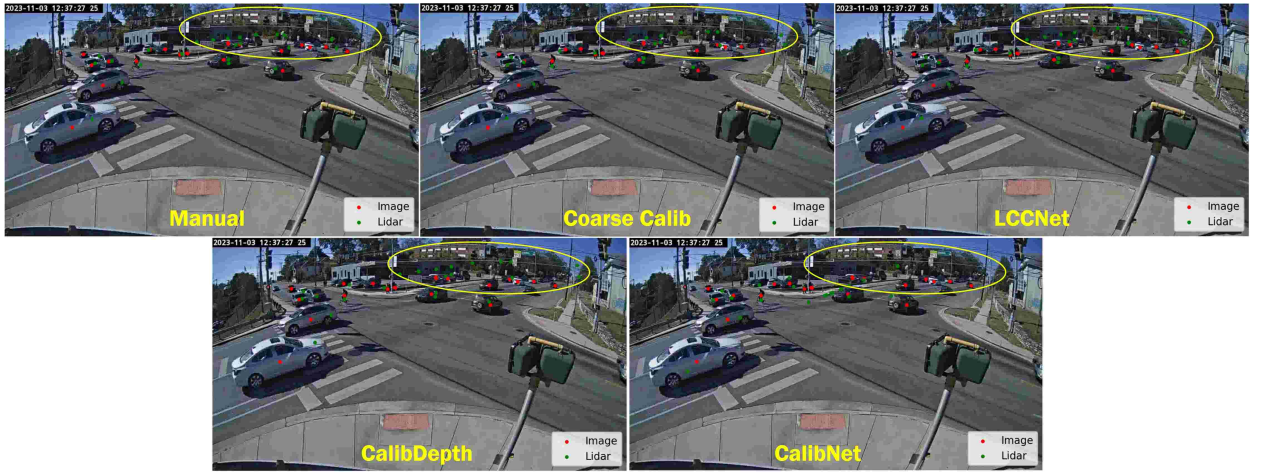


Figure 9: Example Images showing Calibration Results from Coarse Calibration and Other Methods.

and gradually decaying to a minimum learning rate of 0.00001. To further enhance training stability, an exponential moving average (EMA) strategy with a decay rate of 0.9999 was adopted.

Both datasets were divided into training, validation, and test sets, with 90% allocated to the training-validation split and 10% reserved for testing. Within the training-validation split, 90% was designated for training and 10% for validation. Both the training and validation sets were shuffled before each epoch to ensure robust learning. No data augmentation techniques were used, except for resizing to fit the model requirements. For the Common Feature Discriminator, training was conducted over 300 epochs with a batch size of 4. For the Attention-based Model, the training spanned 800 epochs with a batch size of 8, and the token length was set to 256.

4.3. Results and Discussion

4.3.1. Coarse Calibration with Common Feature Discriminator

LiDAR–camera extrinsic calibration fundamentally relies on establishing point correspondences by identifying the same objects in both sensor views. Conventionally, one might manually compare camera images with LiDAR data to locate matching targets, but this process is time-consuming, labor-intensive, and prone to error—particularly given the sparse and texture-limited nature of LiDAR data compared to camera imagery. To address these challenges, we develop a Common Feature Discriminator that automatically detects and associates the same objects from both LiDAR scans and camera frames, thereby generating the point pairs needed for calibration.

Table 2

Performance Comparison of Coarse Calibration and Other Methods

	Manual		Coarse		LCCNet		CalibDepth		CalibNet	
	\mathcal{E}_{AED}	$\mathcal{E}_{\text{RMSE}}$	\mathcal{E}_{AED}	$\mathcal{E}_{\text{RMSE}}$	\mathcal{E}_{AED}	$\mathcal{E}_{\text{RMSE}}$	\mathcal{E}_{AED}	$\mathcal{E}_{\text{RMSE}}$	\mathcal{E}_{AED}	$\mathcal{E}_{\text{RMSE}}$
Dataset 1	131.04	111.57	134.74	114.64	133.55	115.65	137.94	118.12	140.82	126.91
Dataset 2	40.79	32.70	36.39	28.72	29.71	24.31	46.57	38.35	53.22	45.03

1) Common Feature Discriminator Performance: Table 1 summarizes the Common Feature Discriminator’s performance on both datasets, revealing consistently strong binary classification accuracies (98.00% and 92.50% for Datasets 1 and 2, respectively). These high scores indicate that the discriminator is highly effective at distinguishing whether pairs of LiDAR and camera detections correspond to the same physical object. Meanwhile, the slightly lower image and LiDAR classification accuracies reflect the inherent variability in each modality’s appearance and point cloud density, as well as the increased complexity of Dataset 2’s urban traffic scenes. Overall, the results confirm that the discriminator robustly balances object-level matching (binary classification) with semantic recognition (modality-specific class labels). Figure 6 further illustrates the model’s qualitative behavior: two distinct objects (“differ”) are correctly identified as different, while two identical objects from different sensor views are consistently classified as “same.” This underlines the model’s robustness when handling variations in object types and poses. Notably, though occasional misclassifications occur—such as trucks being predicted as cars—these errors are relatively rare and do not significantly affect the system’s ability to produce reliable point correspondences.

2) Coarse Calibration Accuracy: Once the Common Feature Discriminator identifies matching objects across LiDAR and camera modalities and the corresponding point pairs are derived (as shown in Fig. 8a), Homography calibration is employed to obtain a coarse calibration matrix. To comprehensively evaluate the accuracy of this coarse solution, we compare it with several existing calibration methods: Manual calibration, LCCNet (Lv et al., 2021), CalibDepth (Zhu et al., 2023), and CalibNet (Iyer et al., 2018). It is worth noting that for Manual calibration, we selected 34 representative point pairs uniformly distributed across the sensors’ fields of view through manual object matching. Due to the time-intensive nature of this process, we did not exhaustively select all possible point pairs. Thus, the manual calibration results presented here represent a typical calibration effort within a reasonable timeframe, rather than a full-effort exhaustive manual optimization. Table 2 presents the results in terms of the reprojection error metrics \mathcal{E}_{AED} and $\mathcal{E}_{\text{RMSE}}$ (defined in Section 3.1). From Table 2, our coarse calibration demonstrates comparable or, in some cases, superior performance compared to other methods. Specifically, the automated coarse calibration outperforms Manual calibration on Dataset 2, although it exhibits a slightly higher reprojection error than Manual calibration on Dataset 1 (as visualized in Fig. 8b). Nevertheless, the significant advantages of the automated approach in real-time operation and reduced human intervention render this trade-off both acceptable and practical. Furthermore, while the coarse method occasionally exhibits slightly higher errors than certain deep learning-based solutions (e.g., LCCNet), it consistently surpasses others (e.g., CalibDepth and CalibNet), underscoring the effectiveness of the proposed strategy. Fig. 9 presents example calibration outcomes, with red dots (camera detections) and green dots (LiDAR detections) projected onto the image plane. Despite some minor misalignments—particularly in the upper portion of the scene (highlighted by the yellow ellipse)—the coarse calibration overall provides a notably tighter alignment between the two sensor views, potentially enabling precise LiDAR-camera fusion in real-world traffic scenarios.

4.3.2. Fine Calibration with Iterative Refinement

Building on the coarse calibration matrix, the iterative refinement process addresses two key objectives: (1) mitigating the imperfect object matching inherent in the coarse calibration’s Common Feature Discriminator, and (2) enhancing calibration accuracy, reliability, and robustness through the iterative integration of additional point pairs into the optimization process. As outlined in Algorithm 1, the method periodically aggregates newly formed point correspondences over successive frames to redo the Homography calibration and updates the calibration matrix whenever a lower reprojection error is achieved.

Tables 3 and 4 detail the reprojection error evolution (using the \mathcal{E}_{AED} metric) at different frame intervals (with an interval of 100 frames in our implementation) for Datasets 1 and 2. In each interval, the algorithm determines

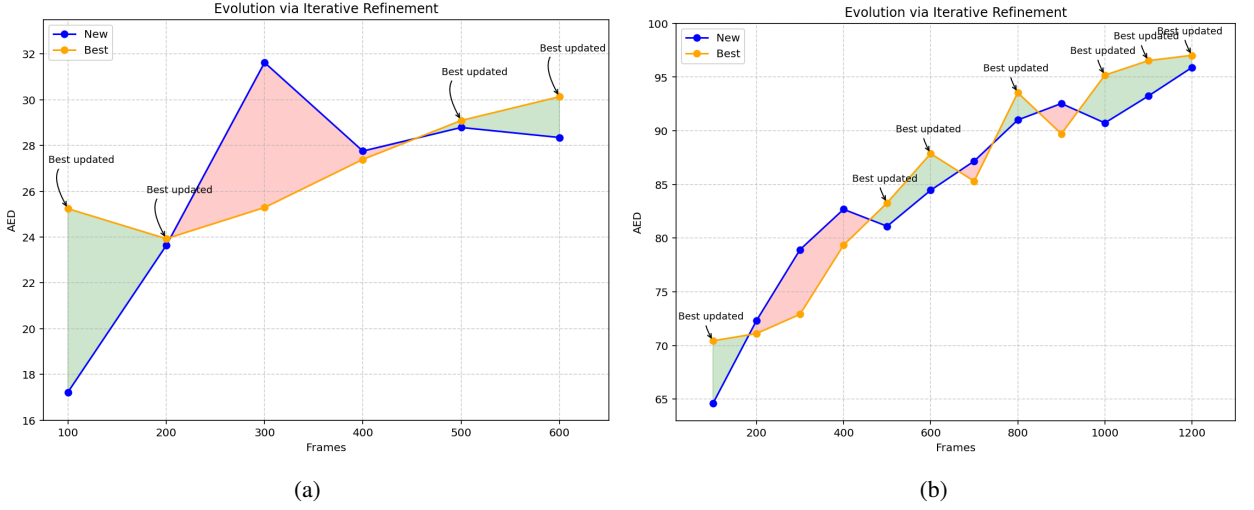


Figure 10: Evolution of \mathcal{E}_{AED} over Frames during Iterative Refinement: (a) on Dataset 1, (b) on Dataset 2. Green-shaded areas indicate \mathcal{E}_{AED} improvement (Best matrix updated); Red-shaded areas indicate \mathcal{E}_{AED} degradation (Best matrix unchanged).

Table 3

Reprojection Error Evolution in Iterative Refinement for Dataset 1

Frame Interval	\mathcal{E}_{AED} (New)	\mathcal{E}_{AED} (Best)	Best Updated
0–100	17.2232	25.2391	Yes (Best \leftarrow New)
0–200	23.6301	23.9287	Yes (Best \leftarrow New)
0–300	31.6232	25.2909	No
0–400	27.7557	27.3924	No
0–500	28.7860	29.0907	Yes (Best \leftarrow New)
0–600	28.3482	30.1302	Yes (Best \leftarrow New)

whether the newly computed homography matrix (*New*) provides a tighter alignment than the previously best-known matrix (*Best*); if so, it updates the calibration accordingly. Fig. 10a and 10b visualize these updates, where the blue line denotes the error obtained from the newly recalibrated matrix in each iteration, and the orange line tracks the evolving best-known solution. Not every recalibration step yields an improvement—reflecting the inherent noise and variability of real-world data—but key frame intervals (e.g., 0–100 for Dataset 1 and 0–1000 for Dataset 2) demonstrate significant error reductions, confirming that the iterative approach converges toward a more accurate solution over time. These updates demonstrate the iterative optimization process’s ability to adaptively refine the calibration as additional data and correspondences become available, ultimately enabling the iterative refinement to achieve significantly higher accuracy compared to the initial coarse calibration (as shown in Fig. 12b).

Fig. 11 provides a more detailed view of how the iterative refinement process unfolds over six iterations, as LiDAR point trajectories are progressively better aligned with camera detections. In Iteration-1, noticeable offsets appear in the vehicle on the left side and for several distant cars near the center of the scene, indicating that the initial coarse calibration matrix is not sufficiently accurate for all regions. By Iteration-2, however, there is a conspicuous improvement: the LiDAR points more precisely cluster around the corresponding vehicles—particularly the trajectory highlighted by the yellow ellipse—demonstrating that additional correspondences acquired in this step already correct many of the early misalignments. Over Iteration-3 and -4, the algorithm refines the alignment further, as the expanded pool of object correspondences helps correct lingering calibration errors, especially for vehicles at varying distances. Finally, by Iteration-5 and -6, the calibration has converged to a state where the majority of LiDAR returns closely

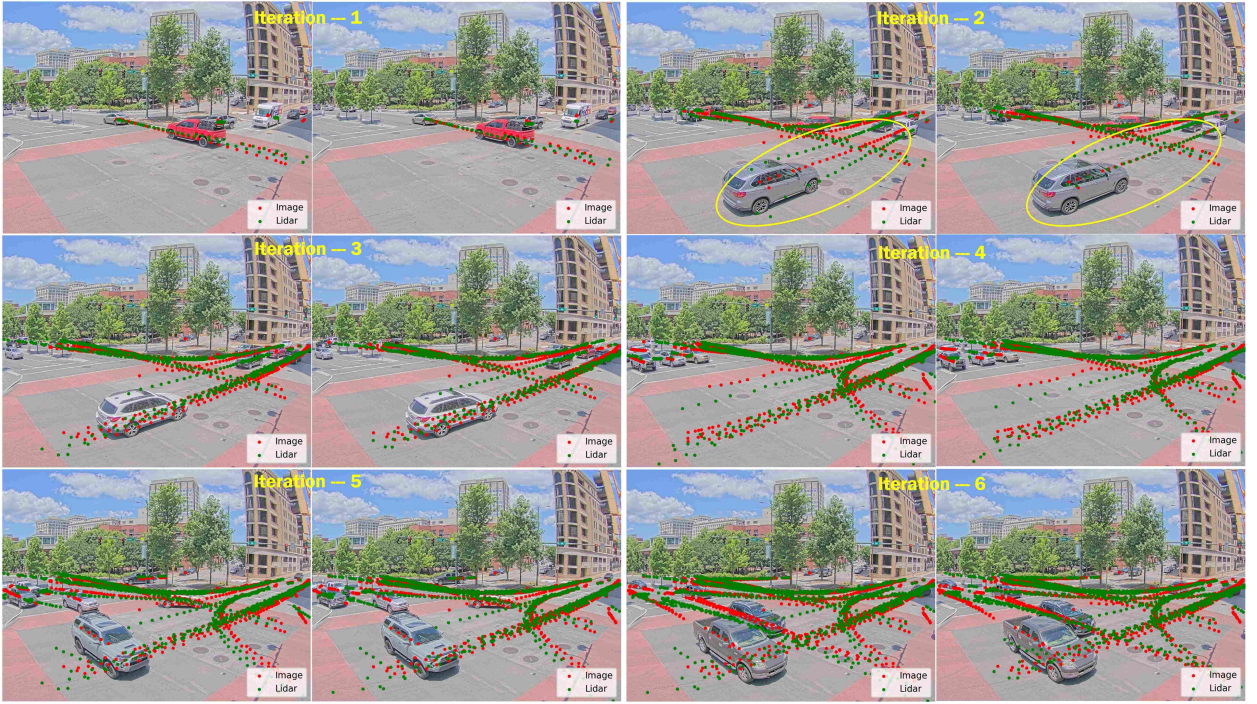


Figure 11: Trajectory Images illustrating the Calibration Performance Evolution through Iterative Refined Calibration.

Table 4
Reprojection Error Evolution in Iterative Refinement for Dataset 2

Frame Interval	\mathcal{E}_{AED} (New)	\mathcal{E}_{AED} (Best)	Best Updated
0–100	64.582	70.423	Yes (Best \leftarrow New)
0–200	72.307	71.101	No
0–300	78.922	72.894	No
0–400	82.678	79.334	No
0–500	81.099	83.277	Yes (Best \leftarrow New)
0–600	84.451	87.872	Yes (Best \leftarrow New)
0–700	87.173	85.293	No
0–800	90.998	93.546	Yes (Best \leftarrow New)
0–900	92.534	89.708	No
0–1000	90.724	95.177	Yes (Best \leftarrow New)
0–1100	93.234	96.532	Yes (Best \leftarrow New)
0–1200	95.891	97.023	Yes (Best \leftarrow New)

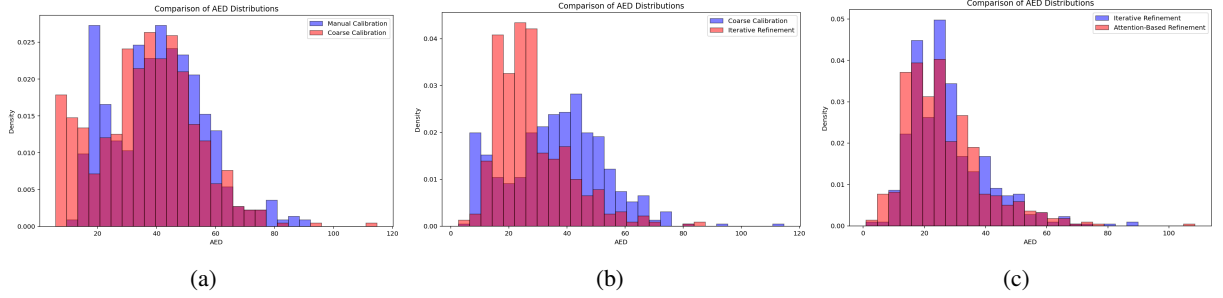
coincide with the camera detections, indicating that additional correspondences spanning a broader field of view substantially improve calibration fidelity.

Table 5 compares the final refined calibration performance with the aforementioned methods. Notably, the iterative refinement outperforms manual calibration by a sizeable margin in both datasets, reducing \mathcal{E}_{AED} from 131.04 to 95.89 in Dataset 1 and from 40.79 to 28.35 in Dataset 2. It also consistently surpasses CalibDepth and CalibNet, while maintaining a competitive edge against LCCNet. These results demonstrate the effectiveness of iteratively incorporating new point correspondences in mitigating decalibrations and refining the sensor alignment. In practice,

Table 5

Performance Comparison of Iterative Refined Calibration and Other Methods

	Manual		Iterative		LCCNet		CalibDepth		CalibNet	
	\mathcal{E}_{AED}	$\mathcal{E}_{\text{RMSE}}$	\mathcal{E}_{AED}	$\mathcal{E}_{\text{RMSE}}$	\mathcal{E}_{AED}	$\mathcal{E}_{\text{RMSE}}$	\mathcal{E}_{AED}	$\mathcal{E}_{\text{RMSE}}$	\mathcal{E}_{AED}	$\mathcal{E}_{\text{RMSE}}$
Dataset 1	131.04	111.57	95.89	74.10	133.55	115.65	137.94	118.12	140.82	126.91
Dataset 2	40.79	32.70	28.35	23.09	29.71	24.31	46.57	38.35	53.22	45.03

**Figure 12:** Comparison of \mathcal{E}_{AED} Distributions on Dataset 2 between: (a) Manual and Coarse Calibration, (b) Coarse and Iterative Refined Calibration, (c) Iterative Refined and Attention-Based Calibration.**Figure 13:** Example Images demonstrating the Performance Improvement of Attention-based Refinement compared to Iterative Refinement.

the procedure offers a compelling balance between accuracy, adaptability, and reduced reliance on strictly supervised or fully manual calibration protocols—making it especially valuable in long-term deployment scenarios.

Overall, the iterative refinement process exhibits several key strengths: 1) **Consistent Refinement:** The reprojection error generally decreases over time, indicating effective optimization. 2) **Adaptability:** The process dynamically updates the calibration matrix when new correspondences improve accuracy, as seen in multiple intervals. 3) **Robustness:** Even during intervals where no improvement occurs, the process maintains a stable calibration without overfitting to potentially noisy correspondences. These findings highlight the iterative refinement’s ability to achieve high-precision calibration, especially in scenarios with sufficient frame data and reliable correspondences. Moreover, it ensures continuous accuracy improvement as more data becomes available, making it a robust solution for real-world applications.

4.3.3. Fine Calibration with Attention-based Refinement

Although the iterative refinement approach already demonstrates strong performance, it remains inherently limited by the planar assumptions of Homography. Our proposed attention-based refinement aims to mitigate errors caused by image distortions and non-planar surfaces. As shown in Table 6, calibration after applying attention-based refinement

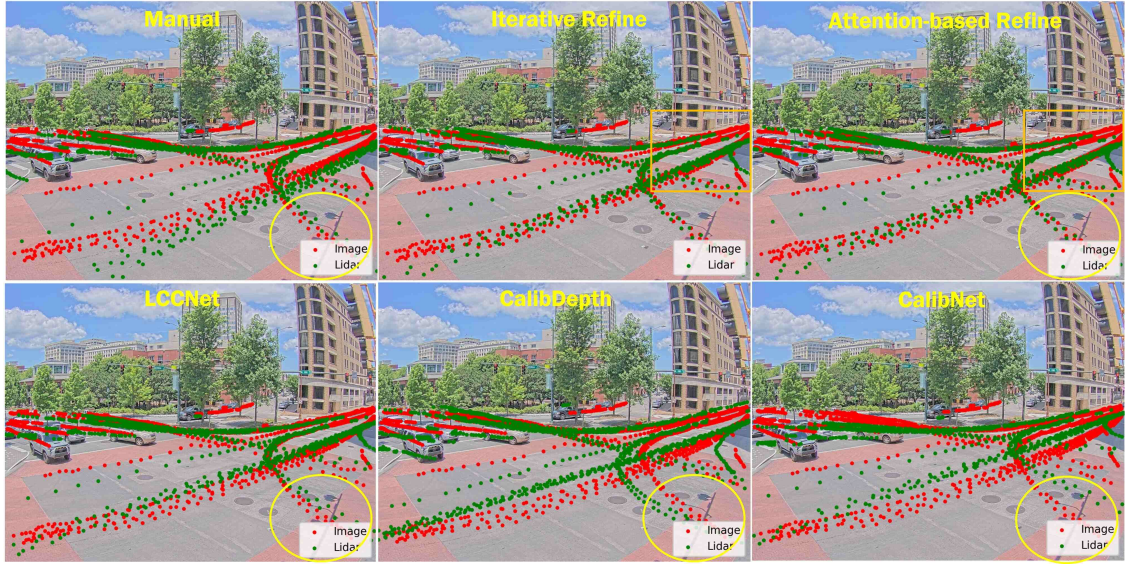


Figure 14: Trajectory Images comparing the Calibration Results after Attention-Based Refinement with Other Methods.

Table 6

Performance Comparison of CalibRefine and Other Methods

	Manual		CalibRefine		LCCNet		CalibDepth		CalibNet	
	\mathcal{E}_{AED}	$\mathcal{E}_{\text{RMSE}}$	\mathcal{E}_{AED}	$\mathcal{E}_{\text{RMSE}}$	\mathcal{E}_{AED}	$\mathcal{E}_{\text{RMSE}}$	\mathcal{E}_{AED}	$\mathcal{E}_{\text{RMSE}}$	\mathcal{E}_{AED}	$\mathcal{E}_{\text{RMSE}}$
Dataset 1	131.04	111.57	93.27	72.68	133.55	115.65	137.94	118.12	140.82	126.91
Dataset 2	40.79	32.70	26.40	22.25	29.71	24.31	46.57	38.35	53.22	45.03

(i.e., CalibRefine) achieves lower reprojection errors than other methods on both datasets, surpassing the iterative refinement (Table 5) in most metrics. Fig. 12c offers a more granular view of these improvements by comparing the \mathcal{E}_{AED} distributions of iterative refinement and attention-based refinement. While the latter still exhibits some overlap with the former, its overall distribution skews toward smaller errors, indicating a more consistently accurate alignment between LiDAR and camera data. Fig. 13 visually illustrates such performance gains of attention-based refinement over iterative refinement.

Fig. 14 further demonstrates the enhancement achieved by Attention-based Refinement compared to other methods in real-world traffic scenes. A closer examination of regions near scene edges and sidewalk corners (highlighted by orange rectangles and yellow circles) reveals that iterative refinement and purely manual alignment often exhibit limitations in accurately aligning distant objects and scene edges. In contrast, Attention-based Refinement more effectively associates LiDAR points with their corresponding objects, particularly under challenging perspective angles. While LCCNet also delivers strong performance, minor misalignments remain visible near scene edges. CalibDepth and CalibNet, however, show even poorer alignment accuracy in these regions. Evidently the improvement margin over iterative refinement is relatively modest, likely due in part to the already high baseline accuracy afforded by iterative methods. Another contributing factor is the inherent limitation of a nine-parameter homography matrix in capturing the full complexity of perspective transformations. These observations highlight both the promise and limitations of the proposed method. More advanced deep learning architectures or more sophisticated mapping mechanisms could better address complex real-world distortions and further improve LiDAR–camera alignment.



Figure 15: Comparison of LiDAR Point Cloud Projection Results on Dataset 1 using Different Calibration Methods.



Figure 16: Comparison of LiDAR Point Cloud Projection Results on Dataset 2 using Different Calibration Methods.

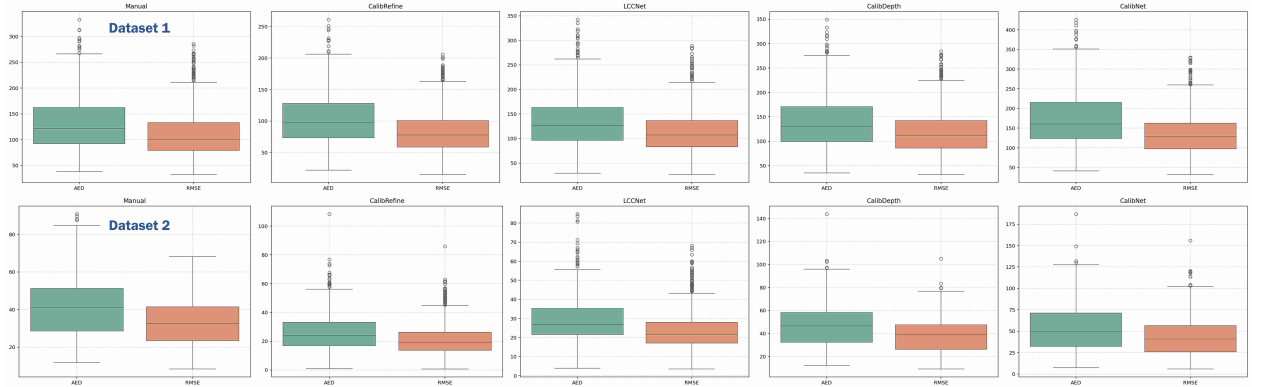


Figure 17: Calibration Error Distributions across Different Methods on Dataset 1 (top row) and Dataset 2 (bottom row).

Overall, our proposed CalibRefine framework consolidates three core components—Coarse Calibration, Iterative Refinement, and Attention-Based Refinement—into a unified solution. As illustrated in Fig. 12, each stage progressively refines the LiDAR–camera alignment, mitigating errors introduced by imperfect correspondence matching (coarse stage), limited point redundancy (iterative stage), or planar homography assumptions (attention-based stage). Table 6 further demonstrates that CalibRefine surpasses existing state-of-the-art methods in terms of quantitative re-projection accuracy. Beyond numerical metrics, Fig. 15 and 16 offer visual validation on Datasets 1 and 2, respectively, revealing how CalibRefine more reliably overlays LiDAR points with their corresponding image objects—particularly at scene edges and larger distances. In addition, Fig. 17 examines the distribution of calibration errors (\mathcal{E}_{AED} and $\mathcal{E}_{\text{RMSE}}$) across competing approaches. Not only does CalibRefine exhibit a lower median error, but the overall spread of high-error outliers is also reduced, indicating its consistent performance. These findings underscore the robustness and adaptability of CalibRefine in real-world traffic environments.

5. Conclusion

In this paper, we presented CalibRefine, an end-to-end, fully automatic, targetless, and online LiDAR–camera calibration framework that integrates three core steps—coarse calibration, iterative refinement, and attention-based refinement—into a unified pipeline. By combining robust object detection with a Common Feature Discriminator, our method circumvents the need for manually placed fiducials or human-labeled sensor parameters. The coarse calibration phase provides a strong initial alignment, which the iterative refinement then continuously improves by leveraging newly acquired point correspondences across frames. Finally, the attention-based stage applies a Vision Transformer and cross-attention to handle non-planar distortions and subtle mismatches beyond the scope of homography.

Experiments on real-world urban datasets confirm that CalibRefine achieves accurate sensor alignment comparable to, and often better than, existing methods. Moving forward, the approach could benefit from exploring more advanced deep learning architectures or sophisticated mapping mechanisms, as well as extending the attention mechanism to incorporate scene geometry. Such enhancements could enable even more precise and high-fidelity calibration, particularly in large-scale deployment scenarios.

Acknowledgments

This work was supported by The Federal Highway Administration (FHWA) Exploratory Advanced Research (EAR) Program. Award No.: 693JJ32350028.

Source Code

Code is available at https://github.com/radar-lab/Lidar_Camera_Automatic_Calibration.

CRedit authorship contribution statement

Lei Cheng: Conceptualization, Formal analysis, Investigation, Methodology, Software, Data curation, Validation, Visualization, Writing –original draft, Writing – review & editing. **Lihao Guo:** Writing – original draft, Writing – review & editing, Data curation. **Tianya Zhang:** Writing – original draft, Writing – review & editing, Software. **Tam Bang:** Writing – review & editing, Software. **Austin Harris:** Writing – review & editing, Data curation. **Mustafa Hajj:** Writing – review & editing, Resources. **Mina Sartipi:** Writing – review & editing, Resources, Project administration, Funding acquisition. **Siyang Cao:** Conceptualization, Writing– review & editing, Validation, Supervision, Project administration, Funding acquisition.

References

- An, P., Ding, J., Quan, S., Yang, J., Yang, Y., Liu, Q., Ma, J., 2024. Survey of extrinsic calibration on lidar-camera system for intelligent vehicle: Challenges, approaches, and trends. *IEEE Transactions on Intelligent Transportation Systems*.
- Beltrán, J., Guindel, C., De La Escalera, A., García, F., 2022. Automatic extrinsic calibration method for lidar and camera sensor setups. *IEEE Transactions on Intelligent Transportation Systems* 23, 17677–17689.
- Berrio, J.S., Shan, M., Worrall, S., Nebot, E., 2021. Camera-lidar integration: Probabilistic sensor fusion for semantic mapping. *IEEE Transactions on Intelligent Transportation Systems* 23, 7637–7652.
- Besser, B., Poloczek, M., 2017. Greedy matching: Guarantees and limitations. *Algorithmica* 77, 201–234.

- Chen, F., Li, L., Zhang, S., Wu, J., Wang, L., 2022. Pbcacalib: Targetless extrinsic calibration for high-resolution lidar-camera system based on plane-constrained bundle adjustment. *IEEE Robotics and Automation Letters* 8, 304–311.
- Cheng, L., Cao, S., 2023. Online targetless radar-camera extrinsic calibration based on the common features of radar and camera, in: NAECON 2023-IEEE National Aerospace and Electronics Conference, IEEE. pp. 294–299.
- Cheng, L., Cao, S., 2025. Transrad: Retentive vision transformer for enhanced radar object detection. *IEEE Transactions on Radar Systems* 1, 1–1. doi:10.1109/TRS.2025.3537604.
- Cheng, L., Sengupta, A., Cao, S., 2023. 3d radar and camera co-calibration: A flexible and accurate method for target-based extrinsic calibration, in: 2023 IEEE Radar Conference (RadarConf23), IEEE. pp. 1–6.
- Cheng, L., Sengupta, A., Cao, S., 2024. Deep learning-based robust multi-object tracking via fusion of mmwave radar and camera sensors. *IEEE Transactions on Intelligent Transportation Systems*.
- Cui, Y., Chen, R., Chu, W., Chen, L., Tian, D., Li, Y., Cao, D., 2021. Deep learning for image and point cloud fusion in autonomous driving: A review. *IEEE Transactions on Intelligent Transportation Systems* 23, 722–739.
- Domhof, J., Kooij, J.F., Gavrila, D.M., 2019. An extrinsic calibration tool for radar, camera and lidar, in: 2019 International Conference on Robotics and Automation (ICRA), IEEE. pp. 8107–8113.
- Domhof, J., Kooij, J.F., Gavrila, D.M., 2021. A joint extrinsic calibration tool for radar, camera and lidar. *IEEE Transactions on Intelligent Vehicles* 6, 571–582.
- Dosovitskiy, A., Beyer, L., Kolesnikov, A., Weissenborn, D., Zhai, X., Unterthiner, T., Dehghani, M., Minderer, M., Heigold, G., Gelly, S., Uszkoreit, J., Hounsby, N., 2021. An image is worth 16x16 words: Transformers for image recognition at scale. URL: <https://arxiv.org/abs/2010.11929>, arXiv:2010.11929.
- Duan, Z., Hu, X., Ding, J., An, P., Huang, X., Ma, J., 2023. A robust lidar-camera self-calibration via rotation-based alignment and multi-level cost volume. *IEEE Robotics and Automation Letters* 9, 627–634.
- Duan, Z., Hu, X., Ding, J., An, P., Huang, X., Ma, J., 2024. A robust lidar-camera self-calibration via rotation-based alignment and multi-level cost volume. *IEEE Robotics and Automation Letters* 9, 627–634. doi:10.1109/LRA.2023.3336250.
- Dubrofsky, E., 2009. Homography estimation. Diplomová práce. Vancouver: Univerzita Britské Kolumbie 5.
- Fu, B., Wang, Y., Ding, X., Jiao, Y., Tang, L., Xiong, R., 2019. Lidar-camera calibration under arbitrary configurations: Observability and methods. *IEEE Transactions on Instrumentation and Measurement* 69, 3089–3102.
- Hartley, R., Zisserman, A., 2003. Multiple view geometry in computer vision. Cambridge university press.
- He, K., Zhang, X., Ren, S., Sun, J., 2015. Deep residual learning for image recognition. URL: <https://arxiv.org/abs/1512.03385>, arXiv:1512.03385.
- Huang, Z., Zhang, X., Garcia, A., Huang, X., 2024. A novel, efficient and accurate method for lidar camera calibration, in: 2024 IEEE International Conference on Robotics and Automation (ICRA), IEEE. pp. 14513–14519.
- Itami, F., Yamazaki, T., 2020. An improved method for the calibration of a 2-d lidar with respect to a camera by using a checkerboard target. *IEEE Sensors Journal* 20, 7906–7917.
- Iyer, G., Ram, R.K., Murthy, J.K., Krishna, K.M., 2018. Calibnet: Geometrically supervised extrinsic calibration using 3d spatial transformer networks, in: 2018 IEEE/RSJ International Conference on Intelligent Robots and Systems (IROS), pp. 1110–1117. doi:10.1109/IROS.2018.8593693.
- Jiang, P., Osteen, P., Saripalli, S., 2021. Semcal: Semantic lidar-camera calibration using neural mutual information estimator, in: 2021 IEEE International Conference on Multisensor Fusion and Integration for Intelligent Systems (MFI), IEEE. pp. 1–7.
- Jiao, J., Chen, F., Wei, H., Wu, J., Liu, M., 2023. Lce-calib: automatic lidar-frame/event camera extrinsic calibration with a globally optimal solution. *IEEE/ASME Transactions on Mechatronics* 28, 2988–2999.
- Jocher, G., 2023. YOLOv8. URL: <https://github.com/ultralytics/ultralytics>. accessed: 2025.
- Koide, K., Oishi, S., Yokozuka, M., Banno, A., 2023. General, single-shot, target-less, and automatic lidar-camera extrinsic calibration toolbox, in: 2023 IEEE International Conference on Robotics and Automation (ICRA), IEEE. pp. 11301–11307.
- Koo, G., Kang, J., Jang, B., Doh, N., 2022. Precise camera-lidar extrinsic calibration based on a weighting strategy using analytic plane covariances. *IEEE Transactions on Instrumentation and Measurement* 71, 1–13.
- Li, X., Duan, Y., Wang, B., Ren, H., You, G., Sheng, Y., Ji, J., Zhang, Y., 2024. Edgecalib: Multi-frame weighted edge features for automatic targetless lidar-camera calibration. *IEEE Robotics and Automation Letters*.
- Li, X., He, F., Li, S., Zhou, Y., Xia, C., Wang, X., 2022. Accurate and automatic extrinsic calibration for a monocular camera and heterogeneous 3d lidars. *IEEE Sensors Journal* 22, 16472–16480.
- Li, X., Xiao, Y., Wang, B., Ren, H., Zhang, Y., Ji, J., 2023. Automatic targetless lidar-camera calibration: a survey. *Artificial Intelligence Review* 56, 9949–9987.
- Luo, Z., Yan, G., Cai, X., Shi, B., 2024. Zero-training lidar-camera extrinsic calibration method using segment anything model, in: 2024 IEEE International Conference on Robotics and Automation (ICRA), IEEE. pp. 14472–14478.
- Lv, J., Zuo, X., Hu, K., Xu, J., Huang, G., Liu, Y., 2022. Observability-aware intrinsic and extrinsic calibration of lidar-imu systems. *IEEE Transactions on Robotics* 38, 3734–3753.
- Lv, X., Wang, B., Dou, Z., Ye, D., Wang, S., 2021. Lccnet: Lidar and camera self-calibration using cost volume network, in: Proceedings of the IEEE/CVF Conference on Computer Vision and Pattern Recognition, pp. 2894–2901.
- Northrop, W., Zhan, L., Haag, S., Zarling, D., et al., 2022. Can Automated Vehicles "See" in Minnesota? Ambient Particle Effects on LiDAR. Technical Report. Minnesota. Department of Transportation. Office of Research & Innovation.
- Ou, N., Cai, H., Wang, J., 2023. Targetless lidar-camera calibration via cross-modality structure consistency. *IEEE Transactions on Intelligent Vehicles*.
- Pandey, G., McBride, J., Savarese, S., Eustice, R., 2012. Automatic targetless extrinsic calibration of a 3d lidar and camera by maximizing mutual information, in: Proceedings of the AAAI conference on artificial intelligence, pp. 2053–2059.

- Park, C., Moghadam, P., Kim, S., Sridharan, S., Fookes, C., 2020. Spatiotemporal camera-lidar calibration: A targetless and structureless approach. *IEEE Robotics and Automation Letters* 5, 1556–1563.
- Peršić, J., Petrović, L., Marković, I., Petrović, I., 2021. Spatiotemporal multisensor calibration via gaussian processes moving target tracking. *IEEE Transactions on Robotics* 37, 1401–1415.
- Petek, K., Vödisch, N., Meyer, J., Cattaneo, D., Valada, A., Burgard, W., 2024. Automatic target-less camera-lidar calibration from motion and deep point correspondences. *arXiv preprint arXiv:2404.17298*.
- Qi, C.R., Yi, L., Su, H., Guibas, L.J., 2017. Pointnet++: Deep hierarchical feature learning on point sets in a metric space. URL: <https://arxiv.org/abs/1706.02413>, arXiv:1706.02413.
- Qiu, Z., Martínez-Sánchez, J., Arias-Sánchez, P., Rashdi, R., 2023. External multi-modal imaging sensor calibration for sensor fusion: A review. *Information Fusion* 97, 101806.
- Rehder, J., Siegwart, R., Furgale, P., 2016. A general approach to spatiotemporal calibration in multisensor systems. *IEEE Transactions on Robotics* 32, 383–398.
- Schneider, N., Piewak, F., Stiller, C., Franke, U., 2017. Regnet: Multimodal sensor registration using deep neural networks, in: 2017 IEEE intelligent vehicles symposium (IV), IEEE. pp. 1803–1810.
- Sengupta, A., Cheng, L., Cao, S., 2022. Robust multiobject tracking using mmwave radar-camera sensor fusion. *IEEE Sensors Letters* 6, 1–4.
- Shang, H., Hu, B.J., 2022. Calnet: Lidar-camera online calibration with channel attention and liquid time-constant network, in: 2022 26th International Conference on Pattern Recognition (ICPR), pp. 5147–5154. doi:10.1109/ICPR56361.2022.9956145.
- Shi, J., Zhu, Z., Zhang, J., Liu, R., Wang, Z., Chen, S., Liu, H., 2020. Calibrcnn: Calibrating camera and lidar by recurrent convolutional neural network and geometric constraints, in: 2020 IEEE/RSJ International Conference on Intelligent Robots and Systems (IROS), IEEE. pp. 10197–10202.
- Strawlab, 2023. Spatial change detection on unorganized point cloud data. URL: https://github.com/strawlab/python-pcl/blob/master/examples/official/octree/octree_change_detection.py. accessed: 2025.
- Sun, C., Wei, Z., Huang, W., Liu, Q., Wang, B., 2022a. Automatic targetless calibration for lidar and camera based on instance segmentation. *IEEE Robotics and Automation Letters* 8, 981–988.
- Sun, Y., Li, J., Wang, Y., Xu, X., Yang, X., Sun, Z., 2022b. Atop: An attention-to-optimization approach for automatic lidar-camera calibration via cross-modal object matching. *IEEE Transactions on Intelligent Vehicles* 8, 696–708.
- Szeliski, R., 2022. Computer vision: algorithms and applications. Springer Nature.
- Taylor, Z., Nieto, J., 2013. Automatic calibration of lidar and camera images using normalized mutual information, in: Robotics and Automation (ICRA), 2013 IEEE International Conference on, Citeseer.
- Tóth, T., Pusztai, Z., Hajder, L., 2020. Automatic lidar-camera calibration of extrinsic parameters using a spherical target, in: 2020 IEEE International Conference on Robotics and Automation (ICRA), IEEE. pp. 8580–8586.
- Verma, S., Berrio, J.S., Worrall, S., Nebot, E., 2019. Automatic extrinsic calibration between a camera and a 3d lidar using 3d point and plane correspondences, in: 2019 IEEE Intelligent Transportation Systems Conference (ITSC), IEEE. pp. 3906–3912.
- Xiao, Y., Li, Y., Meng, C., Li, X., Ji, J., Zhang, Y., 2024. Calibformer: A transformer-based automatic lidar-camera calibration network, in: 2024 IEEE International Conference on Robotics and Automation (ICRA), IEEE. pp. 16714–16720.
- Ye, C., Pan, H., Gao, H., 2021. Keypoint-based lidar-camera online calibration with robust geometric network. *IEEE Transactions on Instrumentation and Measurement* 71, 1–11.
- Yeong, D.J., Velasco-Hernandez, G., Barry, J., Walsh, J., 2021. Sensor and sensor fusion technology in autonomous vehicles: A review. *Sensors* 21, 2140.
- Yin, J., Yan, F., Liu, Y., Zhuang, Y., 2023. Automatic and targetless lidar-camera extrinsic calibration using edge alignment. *IEEE Sensors Journal*.
- Yoon, B.H., Jeong, H.W., Choi, K.S., 2021. Targetless multiple camera-lidar extrinsic calibration using object pose estimation, in: 2021 IEEE International Conference on Robotics and Automation (ICRA), IEEE. pp. 13377–13383.
- Yuan, C., Liu, X., Hong, X., Zhang, F., 2021. Pixel-level extrinsic self calibration of high resolution lidar and camera in targetless environments. *IEEE Robotics and Automation Letters* 6, 7517–7524.
- Yuan, K., Ding, L., Abdelfattah, M., Wang, Z.J., 2022. Licas3: A simple lidar-camera self-supervised synchronization method. *IEEE Transactions on Robotics* 38, 3203–3218.
- Zhang, B., Rajan, R.T., 2022. Multi-feat: Multi-feature edge alignment for targetless camera-lidar calibration. *arXiv preprint arXiv:2207.07228*.
- Zhang, J., Liu, Y., Wen, M., Yue, Y., Zhang, H., Wang, D., 2023a. L 2 v 2 t 2 calib: Automatic and unified extrinsic calibration toolbox for different 3d lidar, visual camera and thermal camera, in: 2023 IEEE Intelligent Vehicles Symposium (IV), IEEE. pp. 1–7.
- Zhang, X., Xiong, Y., Qu, Q., Zhu, S., Guo, S., Jin, D., Zhang, G., Ren, H., Li, J., 2023b. Automated extrinsic calibration of multi-cameras and lidar. *IEEE Transactions on Instrumentation and Measurement*.
- Zhu, J., Xue, J., Zhang, P., 2023. Calibdepth: Unifying depth map representation for iterative lidar-camera online calibration, in: 2023 IEEE International Conference on Robotics and Automation (ICRA), IEEE. pp. 726–733.